

1 Lithological, petrophysical and seal properties of mass-transport 2 complexes (MTCs), northern Gulf of Mexico

3 Nan Wu¹, Christopher A-L. Jackson¹, Howard D. Johnson¹, David M. Hodgson²

4 ¹Basins Research Group, Department of Earth Science & Engineering, Imperial College, Prince Consort
5 Road, London, SW7 2BP, UK

6 ²School of Earth and Environment, University of Leeds, Leeds, LS2 9JT, UK

7 *Email: n.wu16@imperial.ac.uk

8 Abstract

9 Mass transport complexes (MTCs) are one of the most sedimentologically and seismically
10 distinctive depositional elements in many deep-water depositional systems. Seismic
11 reflection data provide spectacular images of the structure, size, and distribution of MTCs.
12 However, a dearth of borehole data means that there is limited direct calibration of MTC
13 lithology to their petrophysical response, or knowledge of how they may act as hydrocarbon
14 reservoir seals. In this study, we evaluate the lithological and petrophysical properties, and
15 seismic reflection characteristics of three deeply-buried (>2300 m), Pleistocene MTCs in the
16 northern Gulf of Mexico. Using high-quality 3D seismic reflection and borehole data we show
17 that: (i) MTC lithology is highly variable, comprising a mudstone-rich debrite matrix containing
18 large (4.5 km³) deformed sandstone-rich blocks; (ii) generally, MTCs are acoustically faster
19 and are more resistive than lithologically similar (i.e. mudstone-dominated) slope deposits
20 occurring at a similar burial depth; (iii) MTC velocity and resistivity increase with depth, likely
21 reflecting an overall downward increase in the degree of compaction; (iv) the lowermost 15-
22 30 m of the MTCs, which represent the basal shear zones, are characterised by relatively high
23 P-wave velocity and resistivity values due to shear-induced over-compaction; and (v) large,
24 sandstone-rich blocks within one of the MTCs are under-compacted and thus possibly porous,
25 and could therefore act as potential reservoirs or fluid flow conduits. We conclude that
26 detailed analysis of petrophysical data, in particular velocity and resistivity logs, may allow
27 recognition of MTCs in the absence of high-quality seismic reflection data, including explicit
28 identification of the basal shear zone. Furthermore, the relatively thick basal shear zone,
29 rather than the overlying and substantially thicker MTC itself, may form the primary
30 permeability barrier and thus seal for underlying hydrocarbon accumulations.

31 1 Introduction

32 Mass-transport complexes (MTCs) comprise deposits from a range of weakly turbulent to fully
33 cohesive, plug-like sediment gravity flows such as slides, slumps, and debris-flows (Talling et
34 al., 2012). MTCs are one of the most sedimentological and seismically distinctive depositional
35 elements in many deep-water depositional systems, where they may form a key component
36 of the stratigraphic record (Posamentier and Martinsen, 2011). MTCs may represent
37 geohazards, threatening seabed infrastructure, and can generate seabed topography that
38 controls subsequent sediment dispersal patterns (Martinsen, 1989; Hühnerbach and Masson,
39 2004; Solheim et al., 2005; Lee et al., 2007; Sawyer, 2007; Urgeles and Camerlenghi, 2013;
40 Kneller et al., 2016). In addition, MTCs may represent drilling hazards because of
41 unpredictable intraformational pressures, and may form hydraulic seals to sandstone
42 reservoirs (Piper et al., 1997; Shipp, 2004; Sawyer et al., 2009; Algar et al., 2011) or form
43 reservoir themselves (Meckel III, 2011). The composition and distribution of MTCs, and our
44 ability to recognise them in the subsurface, are thus of concern to the hydrocarbon industry.

45 MTCs are typically studied using seismic reflection (e.g. Prather et al., 1998; Posamentier and
46 Kolla, 2003; Frey Martinez et al., 2005; Posamentier, 2005; Moscardelli et al., 2006;
47 Moscardelli and Wood, 2008; Bull et al., 2009; Moernaut and De Batist, 2011; Ortiz-Karpf et
48 al., 2015; Ortiz - Karpf et al., 2016), or outcrop data (e.g. Martinsen et al., 2003; Jackson and
49 Johnson, 2009; Dykstra et al., 2011; King et al., 2011; Shipp et al., 2011; Alves, 2015; Sobiesiak
50 et al., 2016; Hodgson et al., 2018). Seismic reflection data allow determination of the
51 distribution, external geometry, internal structure, and kinematics of MTCs. However, these
52 data do not provide a direct calibration of MTC lithology, which must instead be inferred from
53 seismic facies analysis (Moscardelli et al., 2006; Madof et al., 2009; Perov and Bhattacharya,
54 2011). In contrast, outcrop-based studies permit detailed analysis of MTC structure and
55 lithology, but these exhumed and weathered systems do not permit a direct petrophysical
56 characterisation.

57 Petrophysical and lithological studies of buried MTCs are relatively rare, typically drawing on
58 data collected from shallowly buried (<1400 m) deposits (e.g. Sawyer, 2007; Flemings et al.,
59 2008; Sawyer et al., 2009; Algar et al., 2011; Dugan, 2012). These studies show that MTCs are
60 very fine-grained, and are acoustically faster (and thus denser) and have higher resistivity (and

61 thus lower porosity) than surrounding, in-situ sediment of similar composition (Piper et al.,
62 1997; Shipp, 2004; Sawyer, 2007; Algar et al., 2011; Dugan, 2012). How these properties vary
63 with depth and how deeply-buried MTCs are expressed in petrophysical data at depths of
64 interest to the hydrocarbon industry remains unknown. Using petrophysical data from
65 offshore NW Borneo, Algar et al. (2011) studied several deeply buried MTCs; however, in this
66 example they lacked access to high-resolution 3D seismic data to link seismic facies with
67 petrophysical properties.

68 In this study, we use 3D seismic reflection and borehole data from the Atwater Valley
69 concession of the northern Gulf of Mexico to investigate the relationship between the 3D
70 seismic reflection and petrophysical expression of three deeply buried MTCs. By doing this,
71 we can improve our ability to use such data to predict their subsurface rock properties and
72 associated fluid flow behaviour.

73 2 Geological setting

74 Our study area is located in Block 8 of the Atwater Valley concession, c. 130 km SW of the
75 modern Mississippi delta mouth, and c. 60 km basinward of the Pleistocene shelf edge
76 (Galloway et al., 2000; Galloway, 2001) (Figure 1). Present water depths range from 1150 m
77 in the SE to 650 m in the NW. The northern Mississippi slope comprises a series of salt diapirs
78 and minibasins formed due to flow of the Jurassic Louann Salt (Martin and Bouma, 1982; Peel
79 et al., 1995). This study focuses on Pleistocene sediments preserved within minibasins formed
80 by subsidence into allochthonous salt (Jackson et al., 2018) (Figure 1). During the Early to
81 Middle Pleistocene, the Mississippi River and its tributaries supplied the Mississippi delta,
82 which delivered significant amounts of sediment to the shelf, slope, and basin-floor (Galloway
83 et al., 2000; Galloway, 2008; Galloway et al., 2011). In the Late Pleistocene, the East
84 Mississippi river merged with the Red River, forming a deeply incised, pro-glacial Mississippi
85 valley (Saucier, 1997; Galloway et al., 2000). This valley, and the downdip Mississippi canyon,
86 represented the main conduit for sediment transfer onto the basin floor (Weimer et al., 1998;
87 Galloway et al., 2000; Winker and Booth, 2000).

88 A top salt depth map highlights the main salt structures and minibasins within the study area
89 (Figure 2). This study focuses on the stratigraphic fill of an N-trending, up to 21 km long and
90 10 km wide minibasin that contains a 3.5 km thick succession of Plio-Pleistocene siliciclastics

91 (mini-basin 5; Figure 2). Biostratigraphic data provide a relatively low-resolution age control
92 for the Cenozoic sediments (Figure 3B).

93 3 Dataset and Methods

94 The seismic dataset was acquired in 1995-1998, and reprocessed as a single survey in 2008. It
95 contains a 3D zero-phase, Kirchhoff pre-stack depth-migrated seismic reflection volume, with
96 a vertical sample rate of 10 m, record length of 15 km, and final bin size of 25m x 25 m. Vertical
97 seismic resolution is 17-27 m. The dataset covers an area of approximately 550 km² in the
98 southwestern Mississippi Canyon (MC) and northwestern Atwater Valley (AT) protraction
99 areas of the east-central Gulf of Mexico (Figure 2). A slightly deviated exploration well (AT-8
100 #1 ST) was drilled in 1997 in the east of the study area, encountering a c. 3600 m-thick
101 succession of Pleistocene deep-water clastic succession (Figure 2). The well-log dataset
102 includes measurements of velocity (DT), gamma-ray (GR) and resistivity (RT); these data were
103 calibrated with mud-log and seismic reflection data to infer the lithology and petrophysical
104 properties of the MTCs and their bounding strata.

105 We mapped eight highly reflective, laterally continuous seismic horizons (H0 to seabed; Figure
106 3B), delineating MTCs preserved in minibasin 5. MTCs are imaged using a combination of
107 variance and chaos seismic attribute maps. Variance and chaos attribute maps provide
108 measurement of the discontinuities in seismic data, and are sensitive to stratigraphic and
109 structural variability (Chopra and Marfurt, 2007; Brown, 2011). A seismic-to-well tie allowed
110 the relationship between seismic facies and well-log facies to be determined, including the
111 petrophysical properties of the MTCs. Five MTC-bearing intervals were drilled and logged by
112 AT-8 #1 ST; we analyse three in this study (Figure 3B). Well-log data (i.e., GR, AC and RT) were
113 used to infer the lithology of the MTCs and their bounding strata. Cross-plots were
114 constructed to examine the petrophysical properties variation within MTC-bearing intervals
115 and bounding strata.

116 4 Seismic facies analysis

117 A regional N-trending seismic profile through mini-basin 5 illustrates the geometry of the
118 depocentre and bounding salt structures (Figure 3A). We see two main seismic reflection
119 configurations: (i) *chaotic*, which are interpreted as MTCs (i.e. remobilised strata); and (ii)

120 *continuous*, which are interpreted as in-situ slope deposits (Figure 3C). The seismic facies
121 characteristics of the MTCs (facies 3.1 and 3.2) and slope deposits (facies 1 and 2) are further
122 classified based on a more detailed analysis of the seismic reflection characteristics, and by
123 comparing their expression (e.g. reflectivity and continuity, and their external and internal
124 geometry) with previous seismic facies analysis schemes developed for age-equivalent (i.e.
125 Plio-Pleistocene) deep-water sediments deposited in nearby areas (Prather et al., 1998;
126 Roesink et al., 2004; Sincavage et al., 2004; Madof et al., 2009; Doughty-Jones et al., 2017).
127 The observed seismic facies, and their GR expression, are briefly described here and
128 documented more fully in Table 1, before we provide a more detailed analysis of the
129 petrophysical expression of the MTC-bearing intervals.

130 4.1 Seismic facies 1 (SF1)

131 SF1 comprises sub-parallel to parallel, moderate continuity, high-amplitude reflections.
132 Typically, SF1 is ranging from c. 40-50 m thick, and has flat upper and lower contacts with
133 bounding deposits (Table 1). In logs, SF1 has a blocky, low GR response at its base, and a
134 serrated, higher GR response at its top, displaying an overall fining-upward trend. Based on
135 its log response and previous seismic facies-based studies, we infer that SF1 represents thinly
136 bedded, sandstone-rich (at its base) and mudstone-rich (at its top) deposits, possibly
137 deposited in a channel-levee system or at the fringes of a lobe complex (Table 1). This is
138 consistent with C_{th} facies of Prather et al. (1998), with similar seismic facies being documented
139 by Roesink et al. (2004), Sincavage et al. (2004), and Madof et al. (2009) (i.e. inter-bedded
140 sandstone- and mudstone-rich turbidites).

141 4.2 Seismic facies 2 (SF2)

142 SF2 is ranging from c. 100 m to 170 m thick, bounded by sub-parallel to parallel, relatively
143 continuous, low-to-medium amplitude reflections and comprises laterally continuous,
144 parallel, low- to medium amplitude reflections (Table 1). In log data, SF2 shows a high GR
145 response, suggesting it is mudstone-dominated. Based on its expression in seismic and
146 borehole data, and by comparison to seismic facies interpreted in previous studies, we
147 interpreted SF2 as low-energy, mudstone-rich 'background' slope turbidite deposits and/or a
148 mudstone-dominated hemipelagic drape (Prather et al., 1998; Madof et al., 2009; Perov and
149 Bhattacharya, 2011).

150 4.3 Seismic facies 3.1 (SF3.1)

151 SF3.1 is ranging from c. 150-180 m thick, has a rugose top surface and a flat base (Table 1),
152 and comprises moderately deformed, folded and faulted, medium-to-high amplitude seismic
153 reflections. In log data, SF3.1 is expressed by a bell-shaped GR response, with a fining upward
154 trend near its bottom, and box-shaped, 80-120 m thick intervals of low GR at its middle and
155 top. We tie the lower part of SF3.1 with mudstone-rich deposit (i.e. high GR intervals), and
156 the middle and upper parts with thick, sandstone-rich deposits, inter-bedded with thinly
157 bedded mudstone (i.e. low GR intervals). The abundance of faulting and folding, combined
158 with the rugose upper surface, suggest SF3.1 has been remobilised and transported within a
159 MTC. However, based on previous seismic facies interpretations, which lack folding and
160 faulting, and its log character, we interpret SF3.1 to represent sandstone-rich deposit that
161 originally formed submarine lobes (Mahaffie, 1995; Prather et al., 1998; Posamentier and
162 Kolla, 2003; Posamentier, 2005; Sawyer et al., 2007; Doughty-Jones et al., 2017).

163 4.3 Seismic facies 3.2 (SF3.2)

164 SF3.2 comprises c. 190-270 m thick packages of chaotic, low-to-moderate amplitude seismic
165 reflections. The top of SF3.2 is rugose, whereas its basal contact is relatively flat (Table 1). In
166 log data, SF3.2 is characterised by a serrated, overall high GR response that locally contains
167 sharp-based, box-shaped, low GR intervals (Table 1). The lithology of SF3.2 is therefore
168 interpreted as a mudstone-dominated succession (i.e. high GR intervals) that locally contains
169 sandstone blocks (i.e. low GR intervals). Based on its seismic and log response, and
170 interpretations arising from previous seismic facies-based studies (Prather et al., 1998;
171 Sawyer, 2007; Madof et al., 2009; Perov and Bhattacharya, 2011), we interpret SF3.2 as a
172 mudstone-rich debrite.

173 5. Lithology and distribution of MTCs

174 Minibasin 5 contains five main MTC-bearing intervals (Figure 3B, 3C); in this study, we focus
175 on three representative examples, and we begin by providing a description of their general
176 seismic expression and lithology. In subsequent sections, we synthesize observations from
177 these three MTCs to investigate their detailed petrophysical response, and how this relates
178 to MTC structure and emplacement.

179 5.1 MTC 1

180 *Geometry and seismic facies*

181 MTC 1 is bound by horizon H1 and H2 (Figure 3B). It has a tongue-shaped external form,
182 widening SE away from diapir A (Figure 4A, 4B). MTC 1 is 270 m thick, and thickest in the
183 minibasin centre. A 180 m high, 6 km long ramp separates MTC 1 from an overlying debrite
184 (SF3.2), and an underlying interval the contains folded and faulted blocks (Figure 4C, 4D). The
185 abundance of faulting and folding, combined with scours along the basal surface (Figure 4C),
186 suggest that large blocks were transported within MTC1. These blocks are defined by
187 packages of SF3.1 and SF1 that are 80-180 m thick, 4.5-6.8 km long, and 2-3.6 km wide, and
188 which contain NE-SW-striking thrusts. The well intersects the distal part of MTC 1, where
189 thrusts and folds occur (Figure 4A).

190 *Lithology*

191 MTC 1 is sandstone-rich (SF3.1) near its base and mudstone-rich (SF3.2) at its top (Figure 5A).
192 To better investigate lithology variations associated with the three constituent seismic facies
193 of MTC 1, we generated a cross-plot of shale volume (Vsh) and velocity (Vp) (Figure 5B). This
194 plot shows that: (1) both SF1 and SF3.1 have similar proportions of sandstone-rich and
195 mudstone-rich sediments; SF3.1 contains minor amounts of muddy sandstone, whereas SF1
196 does not; (2) sandstone-rich deposits associated with SF1 and SF3.1 are capped and
197 surrounded by mudstone-rich debrite, an observation also inferred from seismic data (Figure
198 4C, 4D); (3) SF3.2 is mudstone-dominated, can be clearly differentiated from other seismic
199 facies, and is defined by a relatively narrow range of distribution in the cross plot.

200 5.2 MTC 2

201 *Geometry and seismic facies*

202 We infer MTC 2 comprises two temporally separate, debrite-dominated (i.e. SF3.2) deposits
203 (MTC 2.1 and 2.2; Figure 6A, 6B), separated by a through-going seismic horizon H2.2 (Figure
204 6C, 6D). Taken together, MTC 2.1 and 2.2 define an up to 120 m thick, N-trending, lenticular-
205 shaped body that widens slightly towards the north (Figure 6B). Two bodies in the centre of
206 the minibasin, and which have sharp, sub-vertical contacts with MTC 2.1, and are interpreted
207 as remnant blocks (Figure 6C, 6D). The well interests the middle part of MTC 2 where it is
208 dominated by chaotic seismic facies (Figure 6A).

209 *Lithology*

210 The remnant block is mudstone-rich at its base, and comprises sandstone and mudstone
211 towards its top (Figure 7A). Overlying MTCs are mudstone-dominated (MTC 2.1 and 2.2;
212 Figure 7A), although the lithological composition of MTC 2 varies when observed in the cross-
213 plot of shale volume (Vsh) and velocity (Vp) (Figure 7B): (1) SF1 and SF3.2 are mudstone-
214 dominated with a small portion of sandstone-rich deposits, although the former is, overall,
215 more mudstone-rich than the latter; (2) SF2 is mudstone-rich, containing a small portion of
216 muddy sandstone; (3) sandstone-rich deposits associated with SF1 are capped and
217 surrounded by mudstone-rich debrite and undeformed background deposit; a similar
218 stratigraphic relationship is inferred from the seismic data (Figure 6C, 6D).

219 5.3 MTC 3

220 *Geometry and seismic facies*

221 MTC 3 occurs in the centre of the minibasin, is slightly elongate, and trends north (Figure 8A,
222 8B). MTC 3 is bounded by horizon H4 and H4.1 (Figure 3B), is up to 182 m thick, comprises
223 chaotic, moderate-amplitude reflections (SF3.2), and has a flat base and rugose top (Figure
224 8C, 8D). The well intersects the central part of MTC 3 where the region is dominated by
225 chaotic seismic facies (Figure 8A).

226 *Lithology*

227 MTC 3 has a mudstone-rich base and top, and a sandstone-rich middle (Figure 9A). The
228 lithological composition of MTC 3 is further revealed in a cross-plot of Vsh and Vp (Figure 9B).
229 SF3.2 is dominated by sandstone-rich and mudstone-rich deposits, with a small portion of
230 muddy sandstone. The lithology distribution in SF3.2 in MTC 3 is thus similar compared to the
231 same seismic facies in MTC 2, but different to that in MTC 1. Based on seismic and log data,
232 MTC 3 is interpreted as a debrite-dominated MTC containing large sandstone-rich (c. 70 m in
233 thickness) blocks.

234 6 Petrophysical analysis of MTCs

235 6.1 General variations in velocity and resistivity

236 P-wave velocity (Vp) data from within MTCs 1-3 show that: (i) MTCs are generally
237 characterised by an overall downward increase in Vp (e.g. 2340-2487 m, MTC3 in Figure 10A);

238 (ii) mudstone-dominated parts of MTCs are acoustically faster than similar lithologies at
239 similar burial depths (e.g. the mudstone-rich debrite in MTC 3 is acoustically faster than the
240 overlying and underlying background mudstone-rich deposits; 2300-2550 m in Figure 10A);
241 (iii) sandstone-dominated parts of all three MTCs tend to have a relatively low V_p , and are
242 acoustically slower than the overlying and underlying mudstone-rich debrite (see below); (iv)
243 the lowermost 15-30 m of the MTCs, which are invariably mudstone-dominated and which
244 directly overlie the basal shear surface, are 5%-9% and 7-25% acoustically faster than similar
245 material within the overlying MTCs and underlying background deposits, respectively. We
246 interpret this interval to represent the basal shear zone (BSZ), with the overall downward of
247 increasing V_p likely to reflect increased compaction and density, and therefore velocity with
248 depth (Figure 10A). The reasons for the sharp increase in V_p just above the MTC basal shear
249 surface is discussed further below.

250 Resistivity (RT) log data show that: (i) RT increases downward within MTCs, but decreases
251 downward in lithologically similar slope deposits in bounding intervals (e.g. increases from
252 2770-2890 m in MTC2, and decreases from 2890-3080 m in the underlying remnant block,
253 Figure 10B); (ii) mudstone-rich debrite (SF3.2) are typically more resistive compared to
254 surrounding, undeformed background deposits at similar burial depths (e.g., 3075-3100 m in
255 MTC1 Figure 10B); (iii) sandstone-dominated parts of all three MTCs tend to have a relatively
256 low RT, and are less resistive than overlying and underlying mudstone-rich debrite (see below);
257 (iv) RT response within MTC 2 and MTC 3 are lower than surrounding, undeformed
258 background deposits; and (v) the lowermost 15-30 m (BSZ) of MTCs are characterised by an
259 RT value that is 15%-25% higher than would be expected by the downward-increasing,
260 'background' RT trend response in the overlying MTC, and 16%-30% higher than underlying
261 and thus more deeply buried, slope background deposits (Figure 14). This finding is consistent
262 with previous studies that suggest that RT increases with depth within MTCs (Shipp, 2004;
263 Dugan, 2012), but is counter to other studies which suggest MTCs are typically more resistive
264 than surrounding sediments (Sawyer et al., 2009; Algar et al., 2011). We explore the reasons
265 for this further in the discussion.

266 6.2 Petrophysical and acoustic characteristics of the basal shear zone

267 The BSZs of all three MTCs are all characterised by negative, medium-to-high amplitude
268 seismic reflections of moderate continuity (Figure 4D, 6C, 8C). For example, the BSZ of MTC 1

269 is more reflective (i.e. -15701 at point 'a' in Figure 11A) than the laterally correlative reflection
270 within flanking background strata (i.e. -4008 at point 'b' in Figure 11A). Because amplitude
271 (i.e. reflectivity) is a function of the reflection coefficient (RC) (i.e. acoustic impedance or 'AI'
272 contrasts) and, ultimately, the acoustic properties of rocks, we can explore what lithological
273 combination and/or variations in their physical properties (e.g. compaction) might give rise
274 to the observed seismic response (equation 1):

$$275 \quad RC = \frac{AI2 - AI1}{AI2 + AI1} \quad (1)$$

276 Where AI1 and AI2 are the sediments overlying and underlying the BSS of MTC 1, respectively
277 (Figure 11B). Because the BSZ of MTC 1 is more consolidated, it is acoustically faster and more
278 resistive than the underlying undeformed deposits (Figure 10A, 10B). AI is a function of
279 acoustic velocity (Vp) and density (ρb) (equation 2):

$$280 \quad AI = Vp * \rho b \quad (2)$$

281 Based on this, AI1>AI2 across the BSS of MTC 1. This illustrates why the amplitude of the BSZ
282 of MTC 1 is not only defined by negative polarity, but is also brighter than that of the laterally
283 correlative, undeformed background deposits.

284 6.3 Petrophysical and acoustic characteristics of sandstone-rich 285 deposit within MTCs

286 MTC 1 has the thickest sandstone-rich interval (c. 170 m). Sandstone-rich intervals of MTC 2.1,
287 2.2 and 3 are up to 30 m, 10 m and 70 m thick, respectively (Table 2).

288 Overall, depth trends in sandstone-rich parts of the MTCs are more variable than in
289 mudstone-rich parts. For example, in contrast to mudstone-rich parts of MTCs where Vp and
290 RT broadly increase with depth (Figure 12A), sandstone-rich parts of MTCs have variable
291 depth trends (Figure 12B). The sandstone-rich parts of three MTCs have lower average Vp and
292 RT values than the mudstone-rich debrite above and below (Figure 13). For example, the
293 average Vp of the sandstone-rich part in MTC 2 at 2140m/s is lower than the Vp of the
294 overlying and underlying mudstone-rich debrites at 2210 m/s and 2240 m/s (Fig 13B). The
295 sandstone-rich part of MTC 3 display an overall increase in Vp and RT with depth (Figure 13A),
296 although the sandstone-rich part of MTC 1 does not vary in Vp and RT with depth (Figure 13C).

297 The petrophysical properties of sandstone-rich parts of MTC 1 are different to those of
298 surrounding mudstone-rich debrite and sandstone-rich deposits in overlying, undeformed
299 background deposits (Figure 13 C). A simplified Vp depth trend can be proposed based on the
300 observed Vp depth trend in Figure 10A. The MTC intervals, except the sandstone-rich blocks
301 in MTC 1, tend to have relatively high pore fluid pressures, which exceed the inferred
302 hydrostatic pressure. This suggests that MTC intervals are more (over)compacted compared
303 to overlying and underlying background slope deposits. Within MTC 1, the Vp trend of the
304 sandstone-rich blocks shifts sharply to a constant low Vp response as compared to the
305 overlying mudstone-rich debrite that has increasing Vp with depth. This indicates that the
306 sandstone-rich blocks of MTC 1 are *less* compacted than the mudstone-rich, debritic matrix.
307 Furthermore, sandstone-rich blocks are only weakly resistive when compared to the overlying
308 mudstone-rich units (Figure 10, Figure 12, Figure 13C). This may suggest that the sandstone-
309 rich blocks in MTC 1 retain higher porosity and are water-saturated.

310 7 Discussion

311 We have characterised: (i) the lithology of relatively deeply buried, seismic-scale MTCs; (ii)
312 the relationship between MTC seismic facies and lithology; and (iii) the petrophysical
313 properties of MTCs, and how they vary with depth and structural position within individual
314 MTCs. Here, we discuss the key implications of our study.

315 7.1 Lithology of MTCs

316 In this study, we demonstrate that significant amounts of sandstone may be present within
317 MTCs. This sandstone can be surprisingly thick (c. 170 m) and contained in relatively
318 homogeneous transported blocks (SF3.2), or relatively thin (10-30 m) and interbedded with
319 mudstone in remobilised lobe and/or channel-fill successions (Table 2). This compositional
320 variability may reflect the different provenance of the MTCs; i.e. from mudstone-rich outer-
321 shelves or slopes lacking sand, or from similar positions that are sandstone-rich due to the
322 presence of deltas or previously deposited, deep-water channel-fills and lobes. This contrasts
323 with the widespread occurrence of argillaceous MTCs, such as those encountered in the
324 Nankai Trough (e.g. Strasser et al., 2012), offshore Angola (e.g. Sikkema and Wojcik, 2000)
325 and in the Gulf of Mexico (e.g. Shipp, 2004; Flemings et al., 2005; Sawyer et al., 2007; Meckel
326 III, 2011).

327 7.2 Petrophysical properties of MTCs

328 *General Petrophysical properties*

329 Prior well-log based studies from IODP and ODP drilling in the Northern Gulf of Mexico (Shipp
330 et al., 2004; Sawyer, 2007; Sawyer et al., 2009; Dugan, 2012; Flemings et al., 2012) and
331 Northwest Borneo (Algar et al., 2011) show that MTCs tend to have a higher Vp, density and
332 RT values than surrounding non-MTC intervals. This reflects the fact that MTCs are more
333 consolidated than their bounding sediments, an observation that is consistent with
334 geotechnical measurements that indicate shear strength increases, whereas water content
335 and void ratio decrease downward within MTCs (Piper et al., 1997; Shipp et al., 2004; Strong,
336 2009; Long et al., 2011; Alves et al., 2014). Physical experiments and theoretical models (e.g.
337 consolidation, fluid-dynamics, and soil-mechanics) confirm that MTCs are denser than
338 bounding strata, typically being densest along their basal shear zone (Major and Iverson, 1999;
339 Sassa et al., 2003; Dugan and Germaine, 2008; Strong, 2009; Meissl et al., 2010).

340 We demonstrate that the three MTCs are more compacted than surrounding background
341 deposits, and that Vp, RT broadly increase downward and with a higher rate as compared to
342 the underlying and overlying un-deformed background sediments. Our findings are thus
343 consistent with observations from Sawyer et al. (2009) and Algar et al. (2011), who show
344 similar downward increase in Vp and RT within individual MTCs. However, RT values are lower
345 than in underlying and overlying undeformed background sediments, except near the MTC
346 basal shear surface. This observation is contrary to previous studies (Shipp, 2004; Sawyer et
347 al., 2009; Dugan, 2012). These authors studied mudstone-dominated MTCs at relatively
348 shallow burial depths (<1400 m), whereas those presented here are relatively sandstone-rich
349 and lie at substantially greater burial depths (>2300 m). Therefore, the differences are
350 attributed to differences in the burial depth and lithology of MTC intervals studied.

351 *Insights into emplacement processes; basal shear surface or zone?*

352 Experimental modelling based studies show that debrites are typically deposited in response
353 to top-down 'freezing' of weakly turbulent, plug-like laminar flows; because the lower parts
354 of these flows are the last to stop deforming they may be more strained (Pickering and Hiscott,
355 2015). Thin section and outcrop data based studies show evidence of liquefaction and
356 fluidization related structures in the lower part of MTC intervals (Ogata et al., 2014). In this

357 study, we show that the lower 15-30 m of the studied MTCs are characterised by relatively
358 high Vp and RT when compared to overlying and underlying deposits. Petrophysical data
359 suggest that, rather than being underlain by a basal shear *surface*, the MTCs overlie basal
360 shear *zone* (BSZ). BSZ thickness and infer strain (based on Vp value) appears to be positively
361 correlated to the thickness of the overlying MTCs; i.e. the thicker the MTCs, the thicker and
362 more strained the BSZs. For example, MTC 3 and MTC 2 are 170 and 83 m thick, with 30 m
363 and 26 m thick BSZs, respectively. Vp values sharply increase at the BSZs by around 20-25%
364 for each MTC, as compared to the overlying debritic sediments of the main MTC body. This
365 contrasts with MTC 1, where the BSZ is only 15 m thick and where Vp increases by only 7%.
366 These differences in Vp may reflect the fact that the well: (i) penetrates different parts of the
367 different MTCs (i.e. the margin of MTC 1 vs. the centre of MTCs 2 and 3), and (ii) penetrates
368 different types of the MTCs (i.e. transported blocks in MTC 1 and debris flow matrix in MTCs
369 2 and 3).

370 Although only one well is available for this analysis, some observations can be made with
371 respect to lateral variability of petrophysical properties (i.e. Vp and RT) within the MTCs. Vp
372 and the thickness of the BSZs appear to vary laterally, being highest beneath the main body
373 of an MTC (i.e. MTC 2 and MTC 3), and lowest in more distal parts (i.e. MTC 1). This suggests
374 that within a single MTC, the BSZ might be thinnest along its margins and thickest beneath its
375 body. However, the thickness and pore pressure of the BSZ might be controlled by other
376 factors, such as: (i) slope angle, which would dictate the momentum of MTCs towards the
377 underlying substrate (i.e. the steeper slope angle, the higher the momentum, and *vice versa*;
378 Algar et al., 2011); (ii) the thickness of the overlying MTC (i.e. BSZ thickness is proportional to
379 the thickness of the overlying MTCs; e.g., MTC 3 is thicker than MTC2, and thus the thickness
380 of BSZ of the former is thicker than that of the latter); (iii) MTC transport mode; the MTCs with
381 fewer blocks (i.e. MTC 2 and 3) will have a thicker BSZs than the MTCs with more transported
382 blocks (MTC 1); (iv) the lithology of the underlying substrate; i.e. a ductile, mudstone-rich
383 substrate may be highly sheared, with the shear stress from the overlying MTCs leading to
384 dewatering rather than erosion of the BSZ (Alves and Lourenço, 2010; Ortiz-Karpf et al., 2017);
385 and (v) bathymetric confinement, which would influence the substrate geometry,
386 heterogeneity, internal characteristics and pathway of MTCs; the thickness of MTCs and their
387 BSZ would thus vary laterally (Ortiz-Karpf et al., 2017).

388 In detail, we suggest the inferred high shear strain characterising the BSZs reflect three stages
389 during MTC emplacement (Figure 14a, b): (i) Phase 1 – high shear stresses within the BSZs
390 cause an increase in fluid pressure beneath the rapidly deposited very fine-grained upper part
391 of the flow; this drives liquefaction within the BSZ (Figure 14c); (ii) Phase 2 – continued
392 shearing drives fluidization and pore fluid expulsion (Figure 14d); and (iii) Phase 3 - as gravity
393 induced shear stress progresses, fluid escape continues to happen, resulting in reduction of
394 pore spaces which then makes the BSZ more compacted (Figure 14e). A key observation is
395 that, even where 30 m thick, the BSZs are too thin to be recognised in seismic reflection data
396 (i.e. these intervals are sub-seismic).

397 *Identifying MTCs using petrophysical data*

398 On the middle to lower slope of the Mississippi fan, GR log data cannot differentiate between
399 MTCs and undeformed background deposits because both are mudstone-rich (i.e. both are
400 characterised by serrated, overall high-GR responses). In this situation, Vp and RT logs may
401 be more useful, as they may present higher values in the MTC debrite than the background
402 deposits, principally because these deposits have undergone some degree of transport, and
403 thus emplacement-related strain and compaction. Our method, which may allow well-based,
404 petrophysically driven mapping of MTCs and their BSZs, can be used in lower-quality 3D
405 seismic datasets that image deep-water sedimentary successions (e.g. sub-salt-canopy
406 minibasins within which seismic resolution is relatively low).

407 7.3 Petroleum implication of MTCs

408 *MTCs as hydrocarbon seals*

409 Most petrophysics-based studies of MTCs indicate these deposits are dominated by
410 mudstone. Furthermore, these studies suggest that, because they are over-compacted, these
411 mudstone-rich MTCs may be better seals than surrounding deposits (Algar et al., 2011). This
412 study suggests that emplacement-related over-compaction in MTCs occurs within the BSZ,
413 meaning this interval may have higher sealing potential than lithologically similar background
414 deposits occurring at similar burial depths. The highly reflective nature of the BSZ of an MTC,
415 which relates to its higher density and acoustic velocity, may thus be an indicator of higher
416 seal potential. The mudstone-rich debrite in the upper part of MTC 1 appears to be a good
417 top and lateral seal for the underlying folded and faulted sandstone-rich transported blocks

418 (Figure 4C, 4D). In MTC 2, the mudstone-rich debrite (MTC 2.1 and MTC 2.2) and the
419 corresponding BSZ may act as a good top and lateral seal for the underlying, sandstone-rich
420 parts of the remnant block (Figure 6C, 6D). In BSZ of MTC 3, which appears to be the most
421 consolidated of all the recognised BSZs, could act as good base seal for underlying sandstone-
422 rich deposits.

423 *Reservoir potential*

424 In this study, we show that sandstone-rich transported blocks can be up to c. 180 m thick,
425 6800 m long, cover 2.5 km² in map-view, and have an approximate volume of 4.5 km³ (i.e.
426 MTC 1). The sandstone-rich parts within remnant blocks underlying MTC 2 are up to 20 m
427 thick, cover 0.0145 km² in map-view, and have an approximate volume of 0.29 km³.
428 Petrophysical data indicate the sandstone-rich blocks within MTC 1 and in the remnant block
429 might be under-pressured and may thus be characterised by relatively high porosities. These
430 transported yet less-deformed sandstone-rich blocks (i.e. MTC 1), and the sandstone-rich
431 parts within the remnant blocks under MTC 2, could be potential reservoirs and may thus be
432 of interest to the hydrocarbon industry (Moore et al., 1995; Alves, 2010; Dunlap et al., 2010;
433 Principaud et al., 2015). In addition and as stated above, the sandstone-rich parts within MTC
434 1 and the remnant blocks are capped by the overlying mudstone-rich deposit, and are
435 externally sealed by the surrounding, mudstone-rich background strata. Intra-MTC blocks of
436 comparable size to those described here (i.e. 1-10 km long, 0.3-2 km wide, 50-500 m thick,
437 and covering an area of 3.63-4 km² have been described by other workers, (e.g., Moscardelli
438 et al., 2006; Ogiesoba and Hammes, 2012).

439 8. Conclusions

440 The petrophysical data and seismic reflection character of three MTCs preserved in a
441 minibasin in the northern Gulf of Mexico indicate that: (i) MTCs are dominated by chaotic,
442 medium-to-low amplitude seismic reflections (debrite), and packages of deformed, but more
443 continuous, medium-to-high amplitude reflections (remnant and transported blocks); (ii)
444 petrophysical data indicate the MTCs are mudstone-dominated, whereas the transported and
445 remnant blocks are relatively sandstone-rich; (iii) MTCs are characterised by high acoustic
446 velocities (as revealed by Vp data) and are relatively more resistive relative to surrounding
447 background sediments at similar burial depths; (iv) the lowermost 15-30 m of the MTCs

448 comprises basal shear zones, which are characterised by relatively high P-wave velocity (V_p)
449 and resistivity (RT) values due to shear-induced over-compaction; (v) V_p and RT vary laterally
450 within the BSZs, being highest in main body of MTC and lower towards the margins; (vi) the
451 hydrocarbon seal potential of MTCs may be internally highly variable, with the BSZ displaying
452 the greatest seal capacity (smallest pore throat diameter and lowest permeability) towards
453 the main body of the MTCs compared to the deposit margins; and (vii) sandstone-rich blocks
454 within the MTC 1 tend to be under-compacted and may maintain anomalously high porosities.
455 Sandstone-rich blocks tend to be internally sealed by overlying mudstone-rich debris and
456 externally sealed by background mudstone-rich deposits.

457 Acknowledgements

458 We thank PGS, in particular Don Herron and Scott Opdyke, for providing the subsurface
459 dataset and allowing the publication of the paper. We would also thank to Harya Nugraha and
460 Michael Steventon who helped us throughout the work.

461

462

463

464

465

466

467

468

469

470

471

472

473

474

475 Figure captions

476 Figure 1. Location map of the study area (red box), showing the position of the modern shelf
477 edge (black dotted line), paleo-shelf edge (white dotted line), and modern depositional
478 systems.

479 Figure 2. Depth map for top salt, showing the overall salt-tectonic structure of the study area.
480 1-5 and A-C refer to minibasins and salt structures, respectively, described in the text.

481 Figure 3. (A) N-trending seismic section showing the overall salt-tectonic structure of the
482 study area. (B) The eight key seismic horizons (H0 to seabed) and main MTC-bearing intervals.
483 (C) The main seismic facies and depositional element interpretation. See Figure 2 for the
484 location of the seismic line. Note the position of well AT-8 #1 ST.

485 Figure 4. (A) Variance map between horizon H1 and 2. The red dot indicates the well location;
486 A-C are salt diapirs referred to in the text. (B) Sketch of MTC 1 indicating some of the key
487 internal structures. Note: (i) the ramp; (ii) the MTC lateral margin; (iii) salt-related normal
488 faults, (iv) intra-MTC thrusts; and (v) transported blocks. (C) WNW-trending seismic profile
489 showing the range of seismic facies within MTC 1 (see figure 4A for location). (D) ENE-trending
490 seismic profile showing the range of seismic facies within MTC 1 (see figure 4A for location).

491 Figure 5. (A) Wireline logs, interpreted lithology, and extracted seismic reflection of MTC 1.
492 Log tracks are gamma ray, acoustic (DTCO1), resistivity (ATR1), lithology interpreted by
493 gamma ray and acoustic log. (B) V_{shale} (V_{sh}) against Velocity (V_p) cross plot for three seismic
494 facies associations within MTC 1. Each seismic facies tend to plot in a distinct cluster with
495 however some dots are plotting away from correlated cluster. Note in Fig. 5A the black dashed
496 lines are top and base boundaries of MTC1, and the black dotted lines are boundaries of each
497 seismic facies. DTCO stands for Delta-Time Compressional (microsec/ft), ATR stands for
498 Attenuation resistivity (deep; ohm-m). The depth is in measured depth.

499 Figure 6. (A) Variance map between horizon H2 and 2.1. The red dot indicates the well location;
500 A-C are salt diapirs referred to in the text. (B) Sketch of MTC 2 indicating some key structures
501 and features. Note: (i) the remnant block, (ii) salt-related normal faults, and (iii) lateral margin.
502 (C) NNE-trending seismic profile showing the range of seismic facies within MTC 2 (see figure

503 4.1 for location). (D) WWE-trending seismic profile showing the range of seismic facies within
504 MTC 2 (see figure 6A for location). The depth is in measured depth.

505 Figure 7. Wireline logs, interpreted lithology, and extracted seismic reflection of MTC 2. Log
506 tracks are gamma ray, acoustic (DTCO1), resistivity (ATR1), lithology interpreted by gamma
507 ray and acoustic log. (B) V_{shale} (Vsh) against Velocity (V_p) cross plot for three seismic facies
508 associations within MTC 2. Each seismic facies tend to plot in a distinct cluster with however
509 some dots are plotting away from correlated cluster. Note in Fig. 7A the black dashed lines
510 are top and base boundaries of MTC2, and the black dotted lines are boundaries of each
511 seismic facies. DTCO stands for Delta-Time Compressional (microsec/ft), ATR stands for
512 Attenuation resistivity (deep; ohm-m). The depth is in measured depth.

513 Figure 8. (A) Chaos map between horizon 4 and horizon 4.1. The red dot indicates the well
514 location; A-C are salt diapirs referred to in the text. (B) Sketch of MTC 3 indicating some key
515 structures and features. Note: (i) the remnant block, (ii) salt-related normal faults, and (iii)
516 lateral margin. (C) WWE-trending seismic profile showing the range of seismic facies within
517 MTC 3 (see figure 8A for location). (D) WWE-trending seismic profile showing the range of
518 seismic facies within MTC 3 (see figure 8A for location). The depth is in measured depth

519 Figure 9. (A) Wireline logs and interpreted lithology of MTC 3. Log tracks are gamma ray,
520 acoustic (DTCO1), resistivity (ATR1), lithology interpreted by gamma ray and acoustic log, and
521 extracted seismic reflection. Note the black dashed lines are top and bottom boundaries of
522 MTC1, black dotted lines are boundaries of each seismic facies. DTCO stands for Delta-Time
523 Compressional (microsec/ft), ATR stands for Attenuation resistivity (deep; ohm-m). (B) V_{shale}
524 against Velocity cross plot for seismic facies 3.2 associations within MTC 3. The depth is in
525 measured depth.

526 Figure 10. (A) Velocity (V_p) log, interpreted lithology column, and a schematic sketch of V_p
527 depth trend. (B) Resistivity (R_t) log and interpreted lithology column. Note that the dotted
528 black line in Figure 10A indicates inferred hydrostatic trend based on V_p log.

529 Figure 11. (A) Amplitude map extracted at basal shear surface of MTC 1 and its correlative
530 surface underlying undeformed strata. Bright amplitude occurs when MTC 1 overlays the
531 surface, and dim amplitude corresponds to the surface underlying undeformed substrate. (B)

532 Schematic cross-section of MTC 1 and its correlative undeformed strata, see location from
533 figure 11A.

534 Figure 12. (A) Velocity (Vp) and Resistivity (Rt) logs of mudstone-rich deposits covering
535 background and MTC deposits. (B) Velocity (Vp) and Resistivity (Rt) logs of sandstone-rich
536 deposits covering background and MTC deposits.

537 Figure 13. (A) Velocity (Vp) and Resistivity (Rt) logs of MTC 3. (B) Velocity (Vp) and Resistivity
538 (Rt) logs of MTC 2. (C) Velocity (Vp) and Resistivity (Rt) logs of MTC 1, see the depth interval
539 from Velocity (Vp) log in Figure 10.

540 Figure 14 a) Schematic sketch of MTC and its basal shear zone; b) schematic sketch of Vp and
541 RT logs within MTC intervals. Schematic sketch of processes within the basal shear zone (see
542 location in a): liquefaction (c); fluid escape (d); overcompaction (e).

543 Table captions

544 Table 1 Summary of seismic facies in minibasin 5, including well logs, lithology, schematic
545 facies geometries, facies characteristics, and depositional environment.

546 Table 2 Approximate dimensions of MTCs by log mapping.

547

548

549

550

551

552

553

554

555

556

557 Reference

558 Algar, S., Milton, C., Upshall, H., Roestenburg, J., and Crevello, P., 2011, Mass-transport deposits of
559 the deepwater northwestern Borneo margin (Malaysia)—Characterization from seismic-
560 reflection, borehole, and core data with implications for hydrocarbon exploration and
561 exploitation: Mass-transport deposits in deepwater settings: Tulsa, Oklahoma, SEPM Special
562 Publication, v. 96, p. 351-366.

563 Alves, T. M., 2010, 3D seismic examples of differential compaction in mass-transport deposits and
564 their effect on post-failure strata: *Marine Geology*, v. 271, no. 3, p. 212-224.

565 -, 2015, Submarine slide blocks and associated soft-sediment deformation in deep-water basins: a
566 review: *Marine and Petroleum Geology*, v. 67, p. 262-285.

567 Alves, T. M., Kurtev, K., Moore, G. F., and Strasser, M., 2014, Assessing the internal character, reservoir
568 potential, and seal competence of mass-transport deposits using seismic texture: A
569 geophysical and petrophysical approach: *AAPG bulletin*, v. 98, no. 4, p. 793-824.

570 Alves, T. M., and Lourenço, S. D., 2010, Geomorphologic features related to gravitational collapse:
571 Submarine landsliding to lateral spreading on a late Miocene–Quaternary slope (SE Crete,
572 eastern Mediterranean): *Geomorphology*, v. 123, no. 1-2, p. 13-33.

573 Brown, A. R., 2011, Interpretation of three-dimensional seismic data, Society of Exploration
574 Geophysicists and American Association of Petroleum Geologists.

575 Bull, S., Cartwright, J., and Huuse, M., 2009, A review of kinematic indicators from mass-transport
576 complexes using 3D seismic data: *Marine and Petroleum Geology*, v. 26, no. 7, p. 1132-1151.

577 Chopra, S., and Marfurt, K. J., 2007, Seismic attributes for prospect identification and reservoir
578 characterization, Society of Exploration Geophysicists and European Association of
579 Geoscientists and Engineers.

580 Doughty-Jones, G., Mayall, M., and Lonergan, L., 2017, Stratigraphy, facies, and evolution of deep-
581 water lobe complexes within a salt-controlled intraslope minibasin: *AAPG Bulletin*, v. 101, no.
582 11, p. 1879-1904.

583 Dugan, B., 2012, Petrophysical and consolidation behavior of mass transport deposits from the
584 northern Gulf of Mexico, IODP Expedition 308: *Marine Geology*, v. 315, p. 98-107.

585 Dugan, B., and Germaine, J. T., 2008, Near - seafloor overpressure in the deepwater Mississippi
586 Canyon, northern Gulf of Mexico: *Geophysical Research Letters*, v. 35, no. 2.

587 Dunlap, D. B., Wood, L. J., Weisenberger, C., and Jabour, H., 2010, Seismic geomorphology of offshore
588 Moroccos east margin, Safi Haute Mer area: *AAPG bulletin*, v. 94, no. 5, p. 615-642.

589 Dykstra, M., Garyfalou, K., Kertzus, V., Kneller, B., Milana, J., Molinaro, M., Szuman, M., and
590 Thompson, P., 2011, Mass-transport deposits: combining outcrop studies and seismic forward

591 modeling to understand lithofacies distributions, deformation, and their seismic expression:
592 Mass-Transport Deposits. SEPM, Tulsa, OK.

593 Flemings, P., Long, H., Dugan, B., Germaine, J., John, C., Behrmann, J. H., Sawyer, D., and Expedition,
594 I., 2008, Pore pressure penetrometers document high overpressure near the seafloor where
595 multiple submarine landslides have occurred on the continental slope, offshore Louisiana,
596 Gulf of Mexico: *Earth and Planetary Science Letters*, v. 269, no. 3, p. 309-325.

597 Flemings, P. B., Behrmann, I., Davies, T., John, C., and Team, E., 2005, Gulf of Mexico hydrogeology—
598 Overpressure and fluid flow processes in the deepwater Gulf of Mexico: Slope stability, seeps,
599 and shallow-water flow: *Integrated Ocean Drilling Program Scientific Prospectus*, v. 308, p. 1-
600 52.

601 Flemings, P. B., John, C., and Behrmann, J., 2012, Expedition 308 synthesis: overpressure,
602 consolidation, and slope stability on the continental slope of the Gulf of Mexico.

603 Frey Martinez, J., Cartwright, J., and Hall, B., 2005, 3D seismic interpretation of slump complexes:
604 examples from the continental margin of Israel: *Basin Research*, v. 17, no. 1, p. 83-108.

605 Galloway, W. E., 2001, Cenozoic evolution of sediment accumulation in deltaic and shore-zone
606 depositional systems, northern Gulf of Mexico Basin: *Marine and Petroleum Geology*, v. 18,
607 no. 10, p. 1031-1040.

608 -, 2008, Depositional evolution of the Gulf of Mexico sedimentary basin: *Sedimentary basins of the*
609 *world*, v. 5, p. 505-549.

610 Galloway, W. E., Ganey-Curry, P. E., Li, X., and Buffler, R. T., 2000, Cenozoic depositional history of the
611 Gulf of Mexico basin: *AAPG bulletin*, v. 84, no. 11, p. 1743-1774.

612 Galloway, W. E., Whiteaker, T. L., and Ganey-Curry, P., 2011, History of Cenozoic North American
613 drainage basin evolution, sediment yield, and accumulation in the Gulf of Mexico basin:
614 *Geosphere*, v. 7, no. 4, p. 938-973.

615 Hodgson, D., Brooks, H., Ortiz-Karpf, A., Spychala, Y., Lee, D., and Jackson, C.-L., 2018, Entrainment
616 and abrasion of megaclasts during submarine landsliding and their impact on flow behaviour:
617 *Geological Society, London, Special Publications*, v. 477, p. SP477. 426.

618 Hühnerbach, V., and Masson, D., 2004, Landslides in the North Atlantic and its adjacent seas: an
619 analysis of their morphology, setting and behaviour: *Marine Geology*, v. 213, no. 1-4, p. 343-
620 362.

621 Jackson, C. A.-L., Zhang, Y., Herron, D. A., and Fitch, P. J., 2018, Subsurface expression of a tertiary salt
622 weld, Gulf of Mexico: *Petroleum Geoscience*, p. petgeo2018-2008.

623 Jackson, C. A., and Johnson, H. D., 2009, Sustained turbidity currents and their interaction with debrite-
624 related topography; Labuan Island, offshore NW Borneo, Malaysia: *Sedimentary Geology*, v.
625 219, no. 1-4, p. 77-96.

626 King, P. R., Ilg, B. R., Arnot, M., Browne, G. H., Strachan, L. J., Crundwell, M., Helle, K., Shipp, R., Weimer,
627 P., and Posamentier, H., 2011, Outcrop and seismic examples of mass-transport deposits from
628 a late Miocene deep-water succession, Taranaki Basin, New Zealand: *Mass-transport deposits*
629 *in deepwater settings: Society for Sedimentary Geology (SEPM) Special Publication 96*, p. 311-
630 347.

631 Kneller, B., Dykstra, M., Fairweather, L., and Milana, J. P., 2016, Mass-transport and slope
632 accommodation: implications for turbidite sandstone reservoirs: *AAPG Bulletin*, v. 100, no. 2,
633 p. 213-235.

634 Lee, H. J., Locat, J., Desgagnés, P., Parsons, J. D., McAdoo, B. G., Orange, D. L., Puig, P., Wong, F. L.,
635 Dartnell, P., and Boulanger, E., 2007, Submarine mass movements on continental margins,
636 *Continental margin sedimentation: from sediment transport to sequence stratigraphy*,
637 Volume 37, Citeseer, p. 213-274.

638 Long, H., Flemings, P., Germaine, J., and Saffer, D., 2011, Consolidation and overpressure near the
639 seafloor in the Ursa Basin, Deepwater Gulf of Mexico: *Earth and Planetary Science Letters*, v.
640 305, no. 1, p. 11-20.

641 Madof, A. S., Christie-Blick, N., and Anders, M. H., 2009, Stratigraphic controls on a salt-withdrawal
642 intraslope minibasin, north-central Green Canyon, Gulf of Mexico: Implications for
643 misinterpreting sea level change: *AAPG bulletin*, v. 93, no. 4, p. 535-561.

644 Mahaffie, M., 1995, Reservoir classification for turbidite intervals at the Mars discovery, Mississippi
645 Canyon Block 807, Gulf of Mexico.

646 Major, J. J., and Iverson, R. M., 1999, Debris-flow deposition: Effects of pore-fluid pressure and friction
647 concentrated at flow margins: *Geological Society of America Bulletin*, v. 111, no. 10, p. 1424-
648 1434.

649 Martin, R. G., and Bouma, A. H., 1982, Active diapirism and slope steepening, northern Gulf of Mexico
650 continental slope: *Marine Georesources & Geotechnology*, v. 5, no. 1, p. 63-91.

651 Martinsen, O., 1989, Styles of soft-sediment deformation on a Namurian (Carboniferous) delta slope,
652 Western Irish Namurian Basin, Ireland: *Geological Society, London, Special Publications*, v. 41,
653 no. 1, p. 167-177.

654 Martinsen, O. J., Lien, T., Walker, R. G., and Collinson, J. D., 2003, Facies and sequential organisation
655 of a mudstone-dominated slope and basin floor succession: the Gull Island Formation,
656 Shannon Basin, Western Ireland: *Marine and Petroleum Geology*, v. 20, no. 6-8, p. 789-807.

657 Meckel III, L., 2011, Reservoir characteristics and classification of sand-prone submarine mass-
658 transport deposits: SEPM Special Publication, v. 96, p. 432-452.

659 Meissl, S., Behrmann, J., and Behrmann, J. H., Data report: preliminary assessment of Pleistocene
660 sediment strength in the Ursa Basin (Gulf of Mexico continental slope) from triaxial and ring
661 shear test data, *in* Proceedings Proceedings of the Integrated Ocean Drilling Program2010,
662 Volume 308.

663 Moernaut, J., and De Batist, M., 2011, Frontal emplacement and mobility of sublacustrine landslides:
664 results from morphometric and seismostratigraphic analysis: *Marine Geology*, v. 285, no. 1-4,
665 p. 29-45.

666 Moore, J. G., Bryan, W. B., Beeson, M. H., and Normark, W. R., 1995, Giant blocks in the South Kona
667 landslide, Hawaii: *Geology*, v. 23, no. 2, p. 125-128.

668 Moscardelli, L., and Wood, L., 2008, New classification system for mass transport complexes in
669 offshore Trinidad: *Basin Research*, v. 20, no. 1, p. 73-98.

670 Moscardelli, L., Wood, L., and Mann, P., 2006, Mass-transport complexes and associated processes in
671 the offshore area of Trinidad and Venezuela: *AAPG bulletin*, v. 90, no. 7, p. 1059-1088.

672 Ogata, K., Mountjoy, J., Pini, G. A., Festa, A., and Tinterri, R., 2014, Shear zone liquefaction in mass
673 transport deposit emplacement: A multi-scale integration of seismic reflection and outcrop
674 data: *Marine Geology*, v. 356, p. 50-64.

675 Ogiesoba, O., and Hammes, U., 2012, Seismic interpretation of mass-transport deposits within the
676 upper Oligocene Frio Formation, south Texas Gulf Coast: *AAPG bulletin*, v. 96, no. 5, p. 845-
677 868.

678 Ortiz-Karpf, A., Hodgson, D., and McCaffrey, W., 2015, The role of mass-transport complexes in
679 controlling channel avulsion and the subsequent sediment dispersal patterns on an active
680 margin: the Magdalena Fan, offshore Colombia: *Marine and Petroleum Geology*, v. 64, p. 58-
681 75.

682 Ortiz-Karpf, A., Hodgson, D. M., Jackson, C. A.-L., and McCaffrey, W. D., 2017, Influence of Seabed
683 Morphology and Substrate Composition On Mass-Transport Flow Processes and Pathways:
684 Insights From the Magdalena Fan, Offshore Colombia: *Journal of Sedimentary Research*, v. 87,
685 no. 3, p. 189-209.

686 Ortiz - Karpf, A., Hodgson, D. M., Jackson, C. A. L., and McCaffrey, W. D., 2016, Mass - Transport
687 Complexes as Markers of Deep - Water Fold - and - Thrust Belt Evolution: Insights from the
688 Southern Magdalena Fan, Offshore Colombia: *Basin Research*.

689 Peel, F., Travis, C., and Hossack, J., 1995, Genetic structural provinces and salt tectonics of the Cenozoic
690 offshore US Gulf of Mexico: A preliminary analysis.

691 Perov, G., and Bhattacharya, J. P., 2011, Pleistocene shelf-margin delta: Intradeltaic deformation and
692 sediment bypass, northern Gulf of Mexico: AAPG bulletin, v. 95, no. 9, p. 1617-1641.

693 Pickering, K., and Hiscott, R., 2015, Deep Marine Systems: Processes, Deposits, Environments, Tectonic
694 and Sedimentation, John Wiley & Sons.

695 Piper, D., Pirmez, C., Manley, P., Long, D., Flood, R., Normark, W., and Showers, W., Mass-transport
696 deposits of the Amazon Fan, *in* Proceedings PROCEEDINGS-OCEAN DRILLING PROGRAM
697 SCIENTIFIC RESULTS1997, NATIONAL SCIENCE FOUNDATION, p. 109-146.

698 Posamentier, H. W., 2005, Stratigraphy and geomorphology of deep-water mass transport complexes
699 based on 3D seismic data, SEG Technical Program Expanded Abstracts 2005, Society of
700 Exploration Geophysicists, p. 2300-2303.

701 Posamentier, H. W., and Kolla, V., 2003, Seismic geomorphology and stratigraphy of depositional
702 elements in deep-water settings: Journal of sedimentary research, v. 73, no. 3, p. 367-388.

703 Posamentier, H. W., and Martinsen, O. J., 2011, The character and genesis of submarine mass-
704 transport deposits: insights from outcrop and 3D seismic data: Mass-transport deposits in
705 deepwater settings: Society for Sedimentary Geology (SEPM) Special Publication 96, p. 7-38.

706 Prather, B. E., Booth, J. R., Steffens, G. S., and Craig, P. A., 1998, Classification, lithologic calibration,
707 and stratigraphic succession of seismic facies of intraslope basins, deep-water Gulf of Mexico:
708 AAPG bulletin, v. 82, no. 5, p. 701-728.

709 Principaud, M., Mulder, T., Gillet, H., and Borgomano, J., 2015, Large-scale carbonate submarine mass-
710 wasting along the northwestern slope of the Great Bahama Bank (Bahamas): Morphology,
711 architecture, and mechanisms: Sedimentary Geology, v. 317, p. 27-42.

712 Roesink, J. G., Weimer, P., and Bouroullec, R., 2004, Sequence stratigraphy of Miocene to Pleistocene
713 sediments of east-central Mississippi canyon, northern Gulf of Mexico.

714 Sassa, S., Miyamoto, J., and Sekiguchi, H., 2003, The dynamics of liquefied sediment flow undergoing
715 progressive solidification, Submarine Mass Movements and Their Consequences, Springer, p.
716 95-102.

717 Saucier, R. T., 1997, Geomorphology and Quarternary Geologic History of the Lower Mississippi Valley.
718 Volume 1.

719 Sawyer, D. E., 2007, Lateral Variations in Core, Log, and Seismic Attributes of a Mass Transport
720 Complex in the Ursa Region, IODP Expedition 308, Northern Gulf of Mexico.

721 Sawyer, D. E., Flemings, P. B., Dugan, B., and Germaine, J. T., 2009, Retrogressive failures recorded in
722 mass transport deposits in the Ursa Basin, Northern Gulf of Mexico: Journal of Geophysical
723 Research: Solid Earth, v. 114, no. B10.

724 Sawyer, D. E., Flemings, P. B., Shipp, R. C., and Winker, C. D., 2007, Seismic geomorphology, lithology,
725 and evolution of the late Pleistocene Mars-Ursa turbidite region, Mississippi Canyon area,
726 northern Gulf of Mexico: AAPG bulletin, v. 91, no. 2, p. 215-234.

727 Shipp, R. C., 2004, Physical Characteristics and Impact of Mass Transport Complexes on Deepwater
728 Jetted Conductors and Suction Anchor Piles.

729 Shipp, R. C., Nott, J. A., and Newlin, J. A., Physical characteristics and impact of mass transport
730 complexes on deepwater jetted conductors and suction anchor piles, *in* Proceedings Offshore
731 Technology Conference 2004, Offshore Technology Conference.

732 Shipp, R. C., Weimer, P., and Posamentier, H. W., 2011, Mass-transport deposits in deepwater settings,
733 SEPM Soc for Sed Geology, v. 96.

734 Sikkema, W., and Wojcik, K. M., 2000, 3D Visualization of Turbidite Systems, Lower Congo Basin,
735 Offshore Angola, *in* Weimer, P., ed., Deep-Water Reservoirs of the World, SEPM Society for
736 Sedimentary Geology.

737 Sincavage, R., Weimer, P., and Bouroullec, R., 2004, Sequence Stratigraphy of Upper-Miocene to
738 Pleistocene Sediments of Southwestern Mississippi Canyon and Northwestern Atwater Valley,
739 Northern Gulf of Mexico.

740 Sobiesiak, M. S., Kneller, B., Alsop, G. I., and Milana, J. P., 2016, Internal deformation and kinematic
741 indicators within a tripartite mass transport deposit, NW Argentina: *Sedimentary Geology*.

742 Solheim, A., Bryn, P., Sejrup, H., Mienert, J., and Berg, K., 2005, Ormen Lange—an integrated study for
743 the safe development of a deep-water gas field within the Storegga Slide Complex, NE Atlantic
744 continental margin; executive summary, Ormen Lange—an Integrated Study for Safe Field
745 Development in the Storegga Submarine Area, Elsevier, p. 1-9.

746 Strasser, M., Henry, P., Kanamatsu, T., Thu, M. K., Moore, G. F., and Expedition, I., 2012, Scientific
747 drilling of mass-transport deposits in the Nankai accretionary wedge: First results from IODP
748 Expedition 333, Submarine mass movements and their consequences, Springer, p. 671-681.

749 Strong, H. E., 2009, The origin and properties of mass transport deposits, Ursa Basin, Gulf of Mexico.

750 Talling, P. J., Masson, D. G., Sumner, E. J., and Malgesini, G., 2012, Subaqueous sediment density flows:
751 Depositional processes and deposit types: *Sedimentology*, v. 59, no. 7, p. 1937-2003.

752 Urgeles, R., and Camerlenghi, A., 2013, Submarine landslides of the Mediterranean Sea: Trigger
753 mechanisms, dynamics, and frequency - magnitude distribution: *Journal of Geophysical
754 Research: Earth Surface*, v. 118, no. 4, p. 2600-2618.

755 Weimer, P., Varnai, P., Budhijanto, F. M., Acosta, Z. M., Martinez, R. E., Navarro, A. F., Rowan, M. G.,
756 McBride, B. C., Villamil, T., and Arango, C., 1998, Sequence stratigraphy of Pliocene and

757 Pleistocene turbidite systems, northern Green Canyon and Ewing Bank (offshore Louisiana),
758 northern Gulf of Mexico: AAPG bulletin, v. 82, no. 5, p. 918-960.

759 Winker, C. D., and Booth, J. R., Sedimentary dynamics of the salt-dominated continental slope, Gulf of
760 Mexico: integration of observations from the seafloor, near-surface, and deep subsurface, *in*
761 Proceedings GCSSEPM Foundation 20th Annual Research Conference, Deep-Water Reservoirs
762 of the World2000, SEPM, p. 1059-1086.

763

764

765

766

767

768

769

770

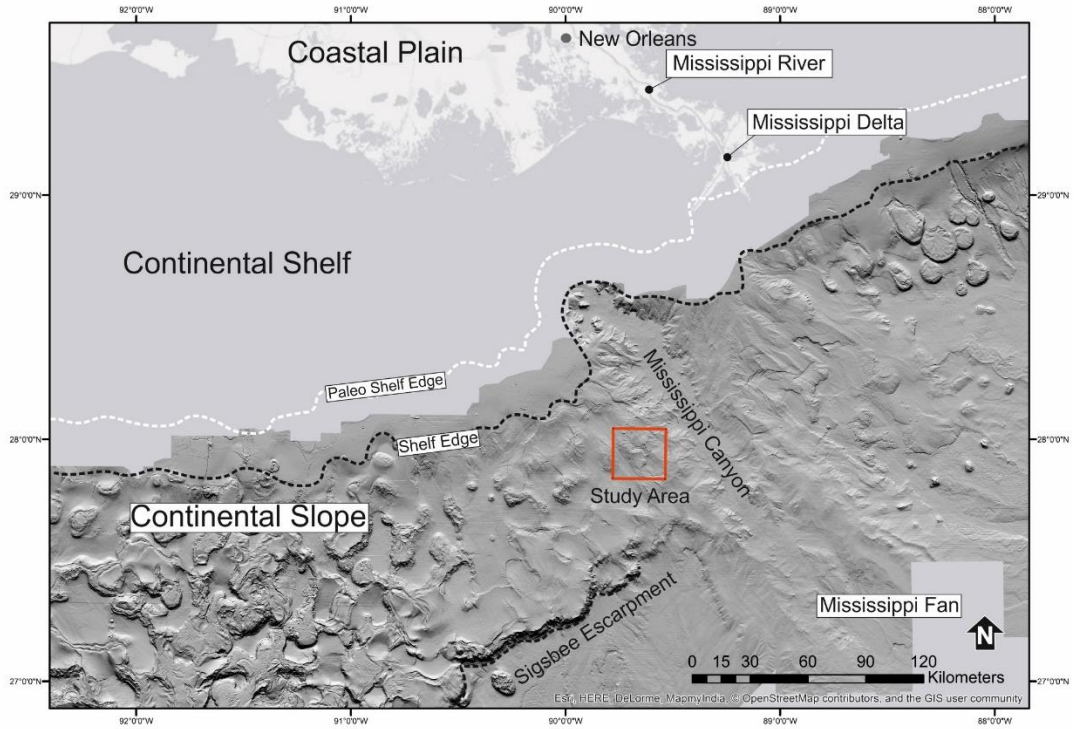
771

772

773

774

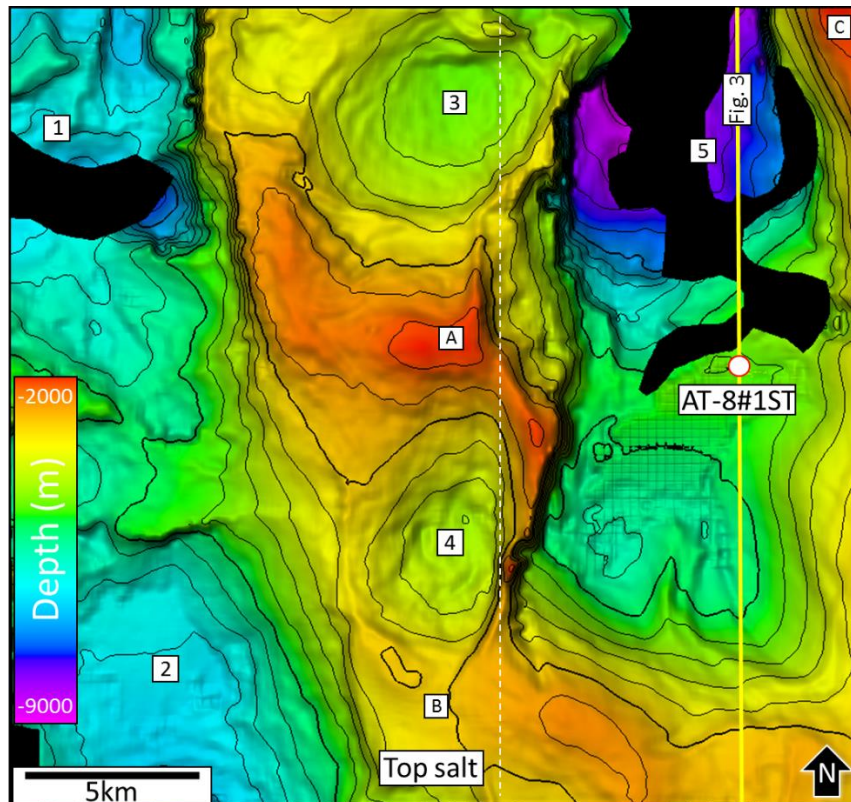
Figure 1



775

776

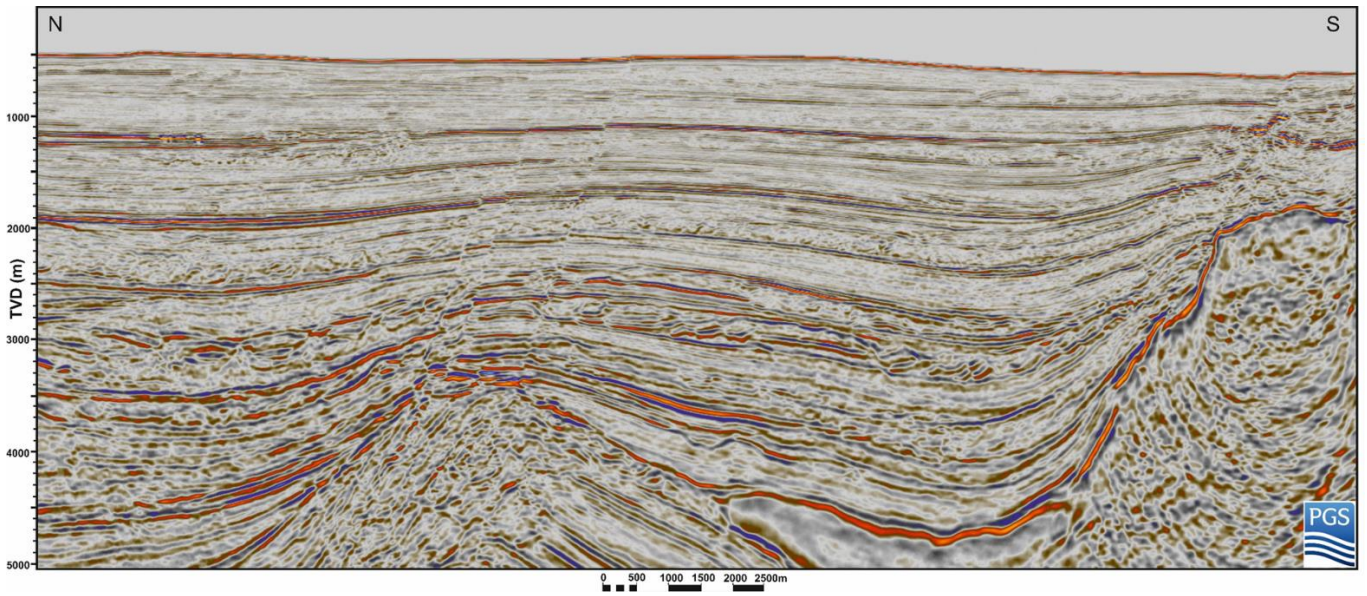
Figure 2



777

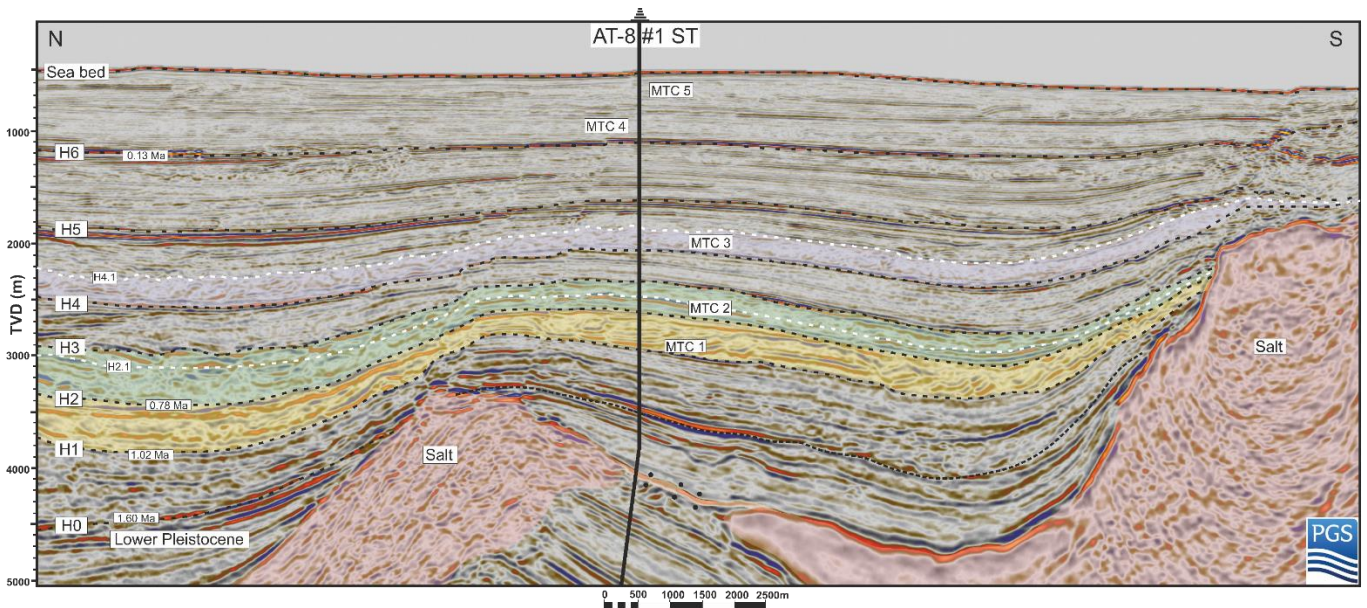
778

779 Figure 3A



780

781 Figure 3B



782

783

784

785

786

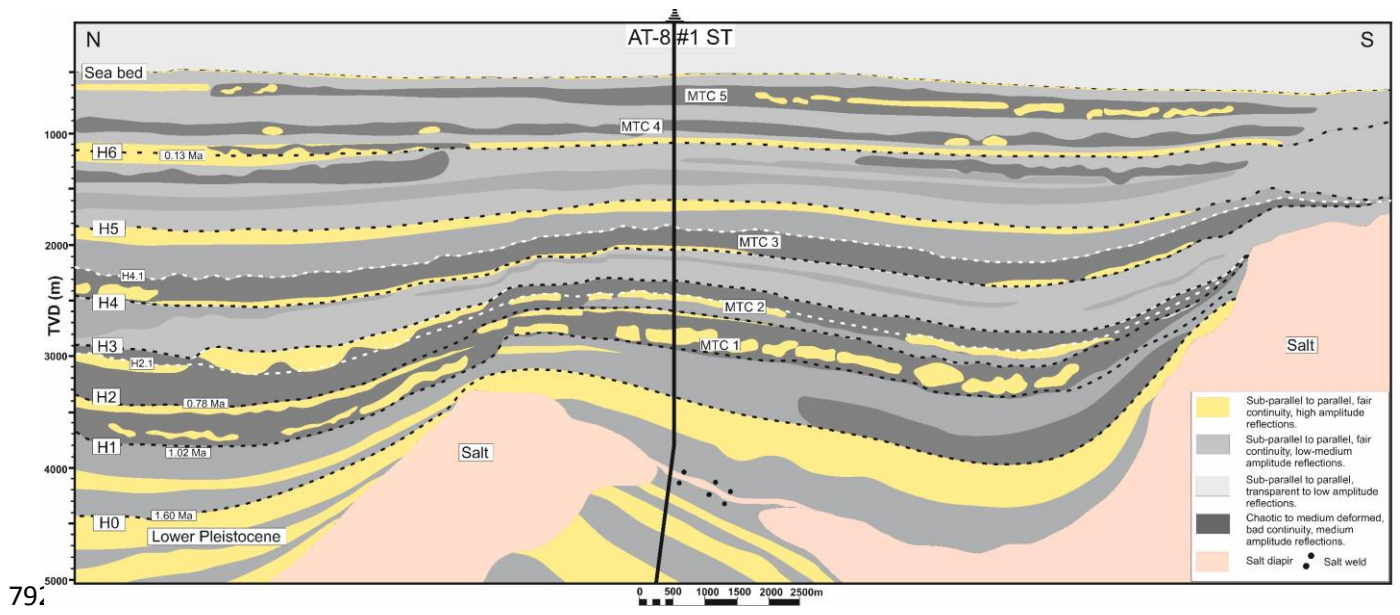
787

788

789

790

791 Figure 3C



79.

Figure 4A

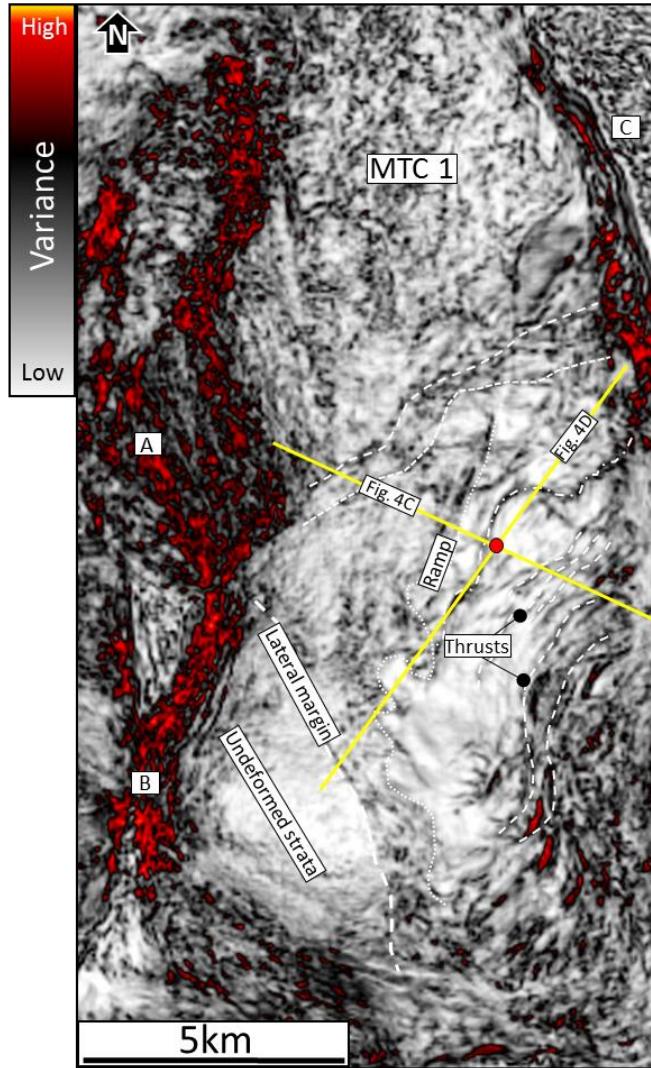
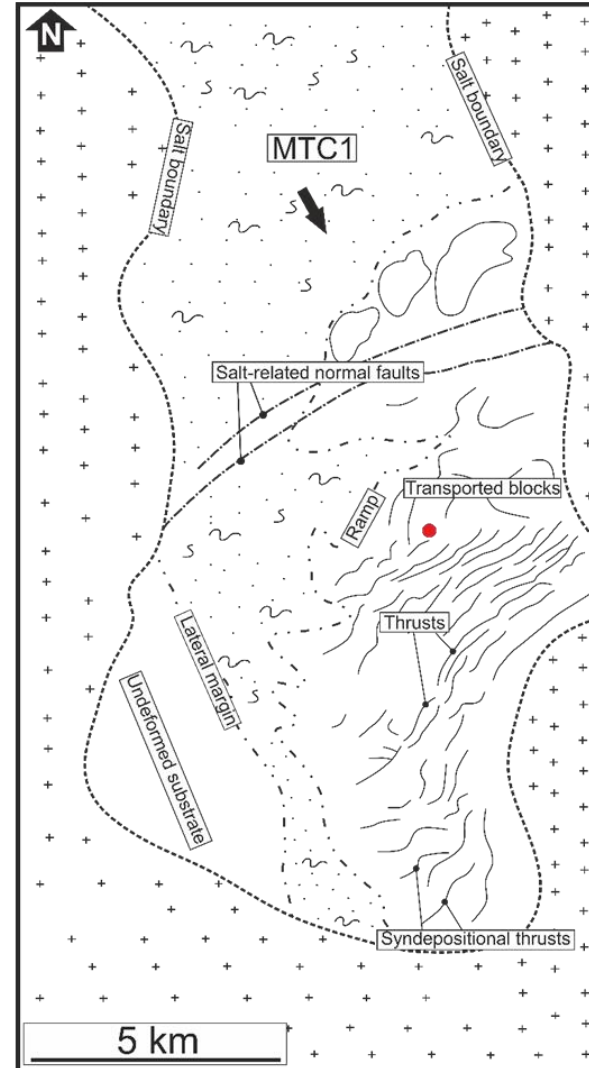
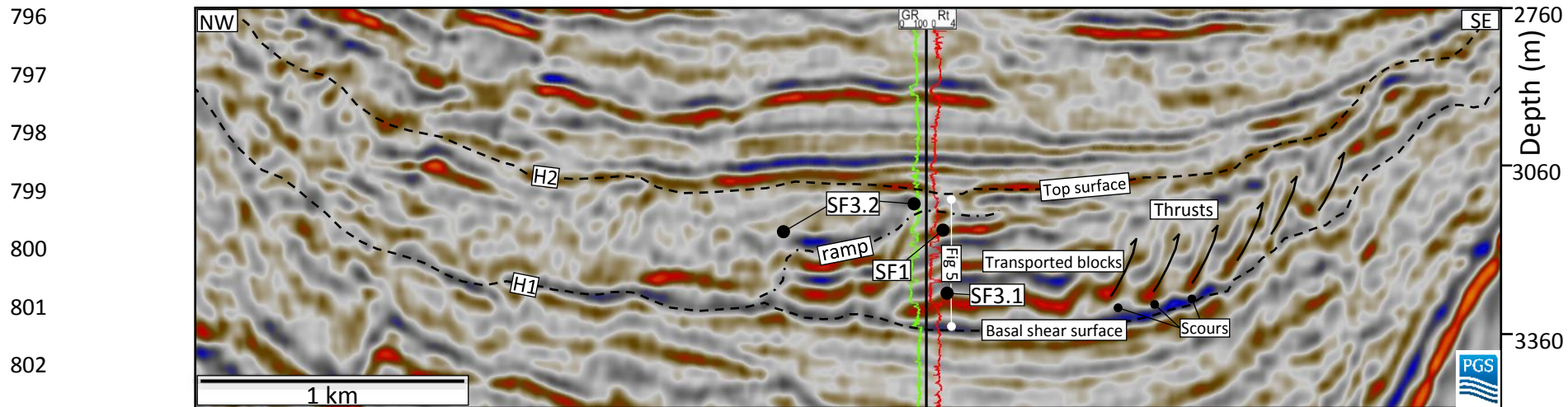


Figure 4B



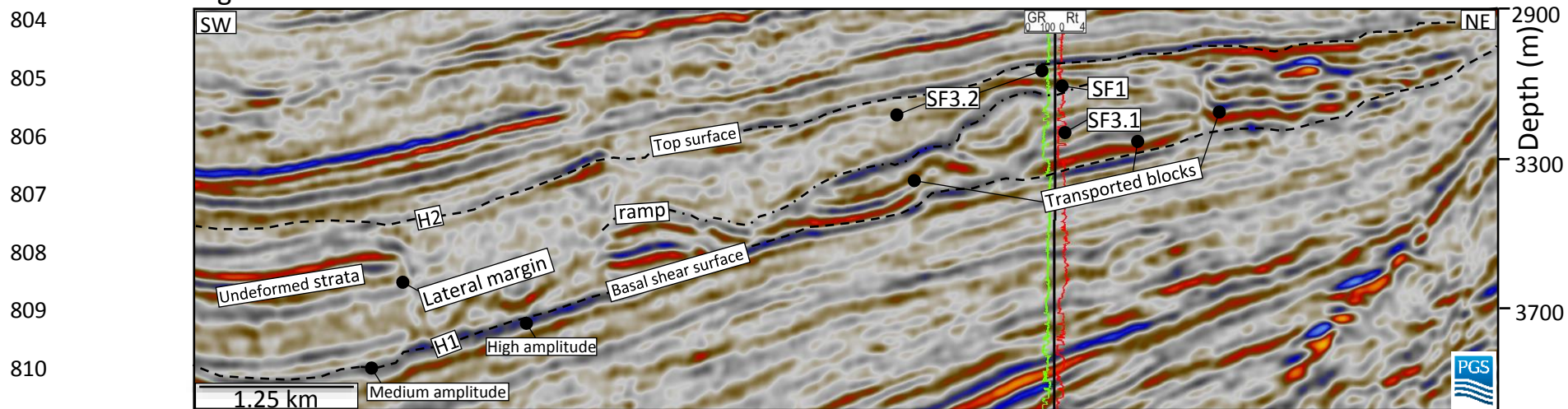
795

Figure 4C



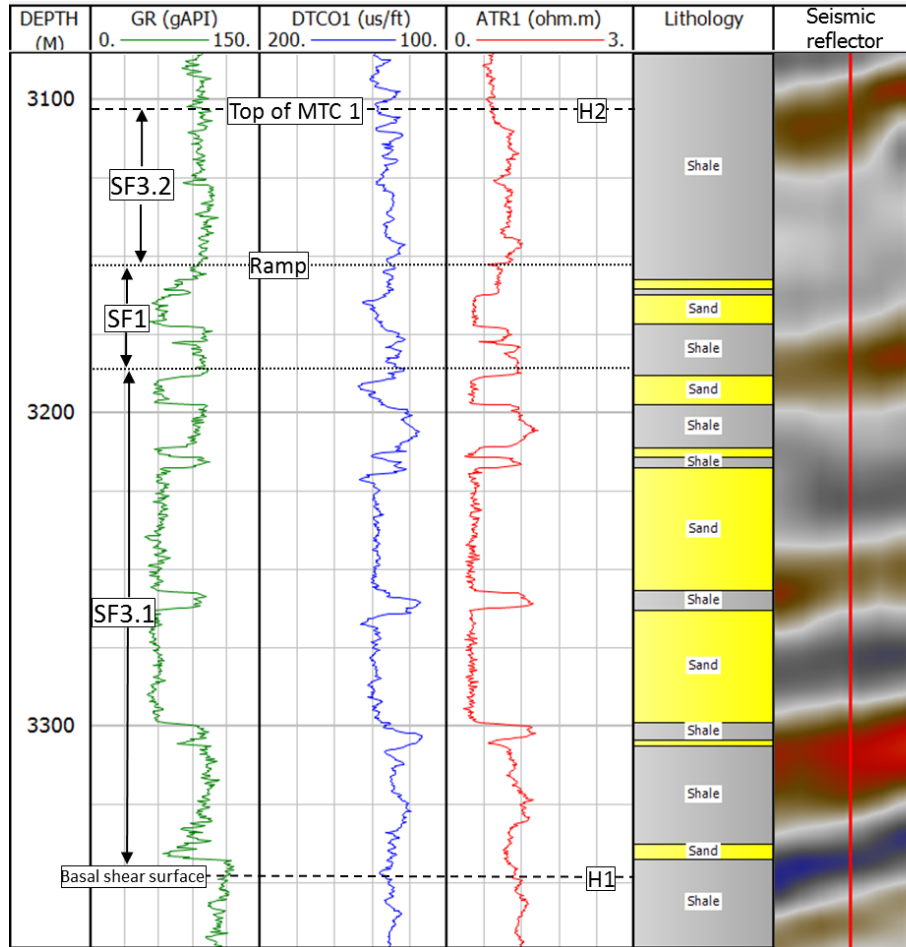
803

Figure 4D



811

812 Figure 5A



813

Figure 5B

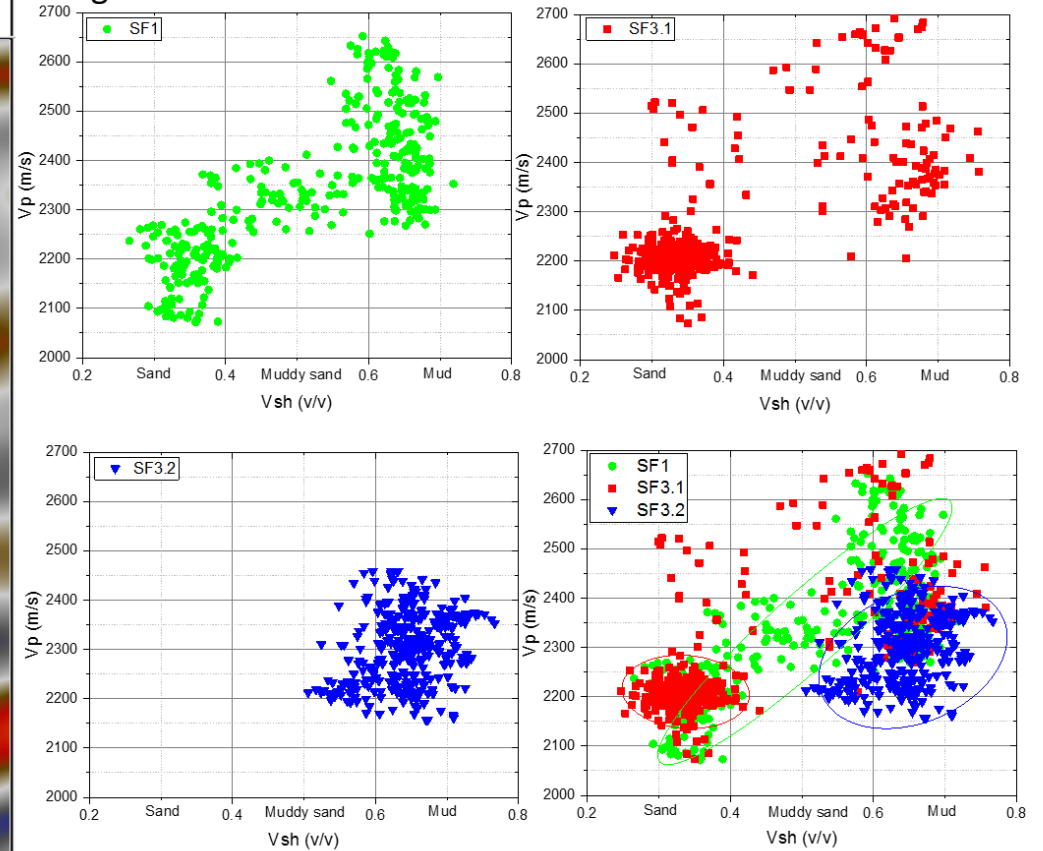
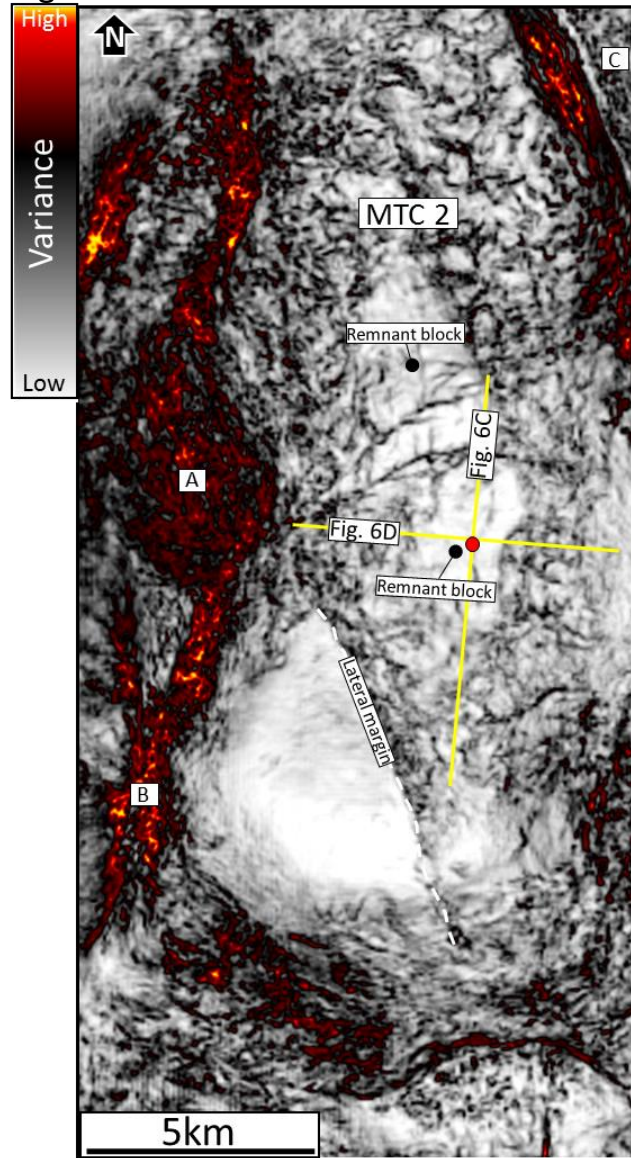
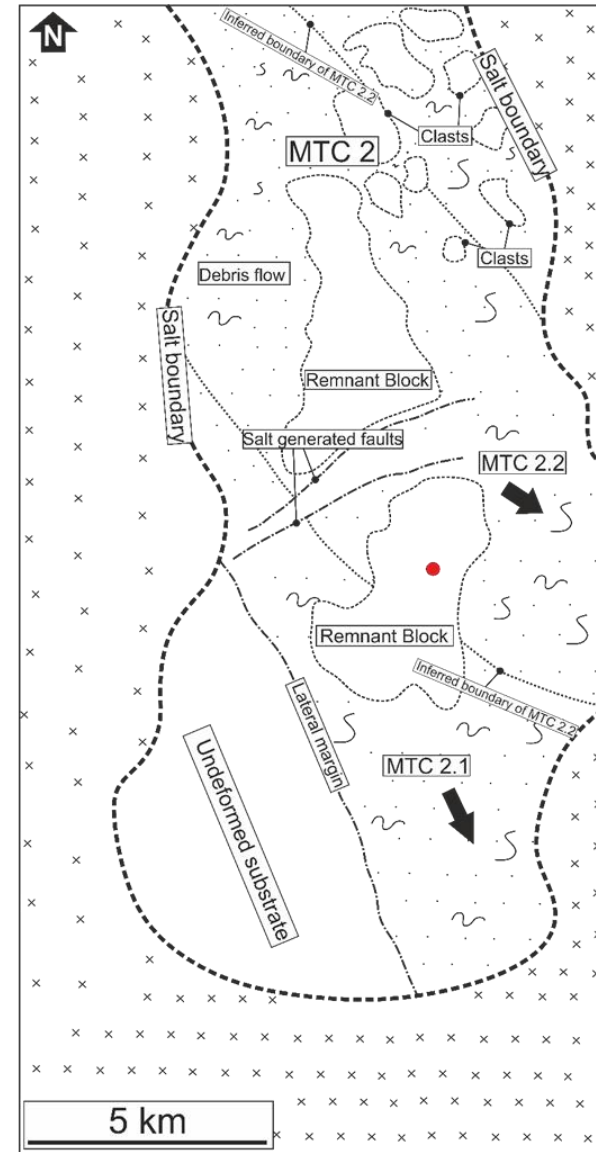


Figure 6A



814

Figure 6B



33

Figure 6C

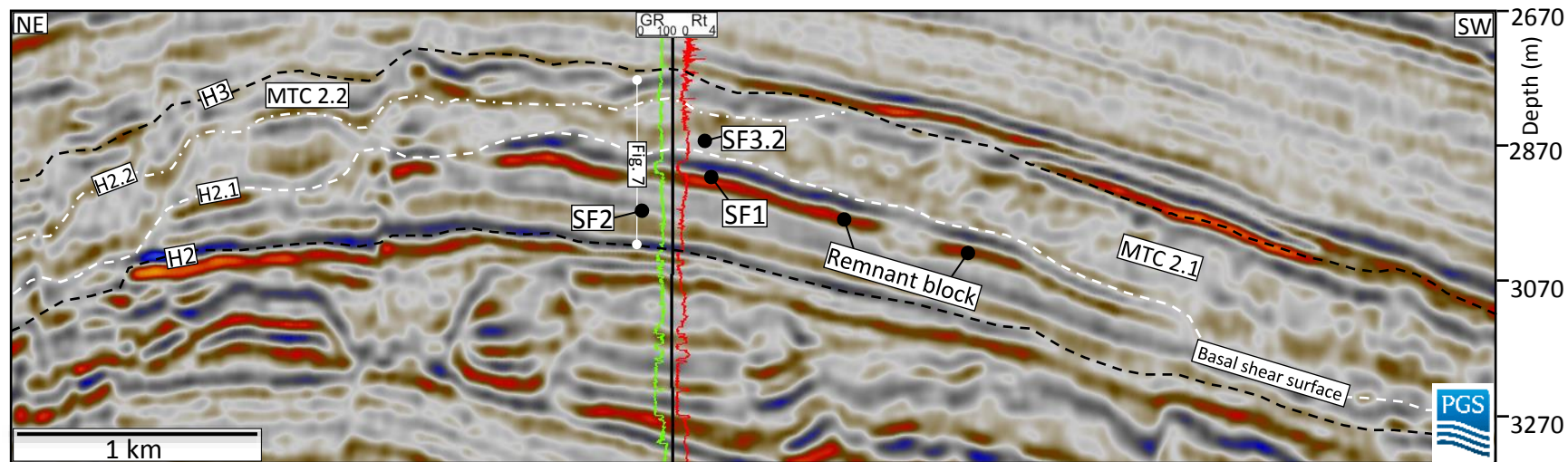


Figure 6D

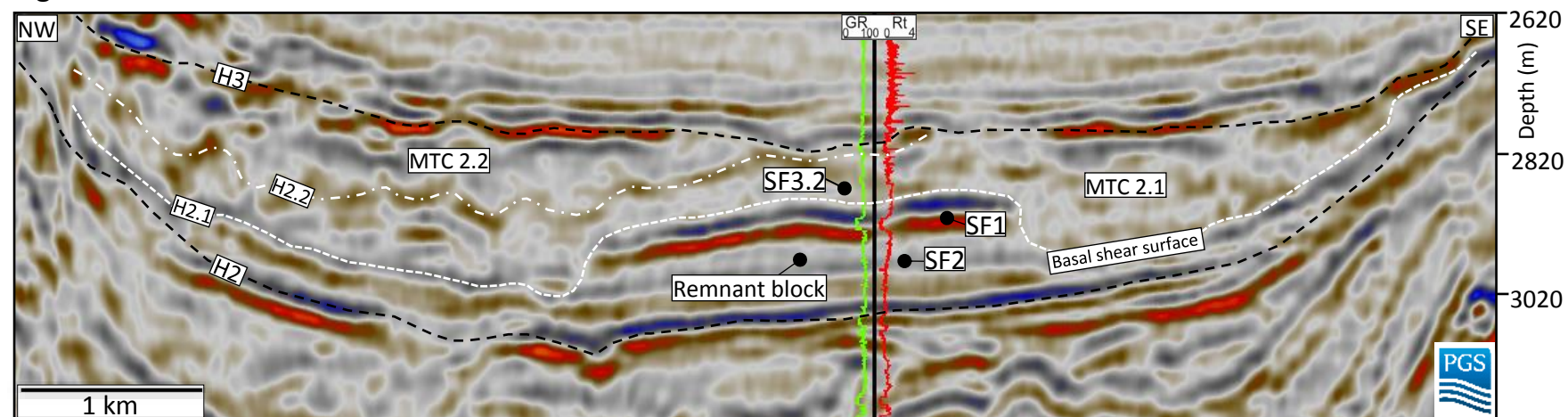


Figure 7A

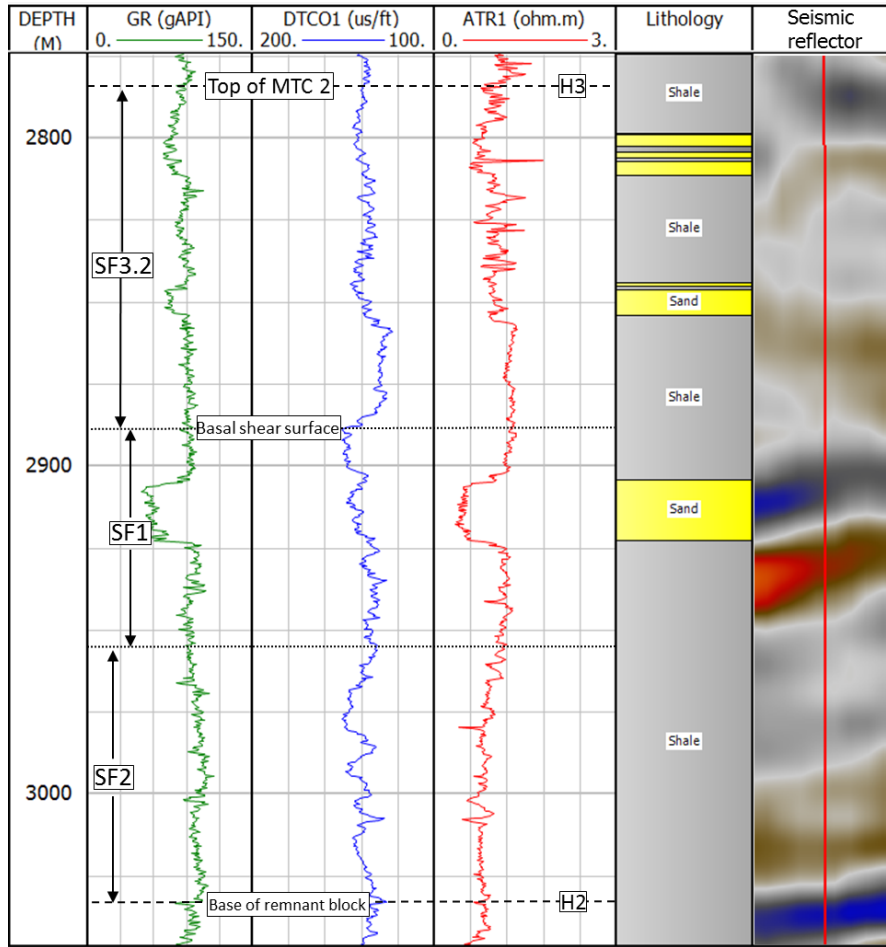


Figure 7B

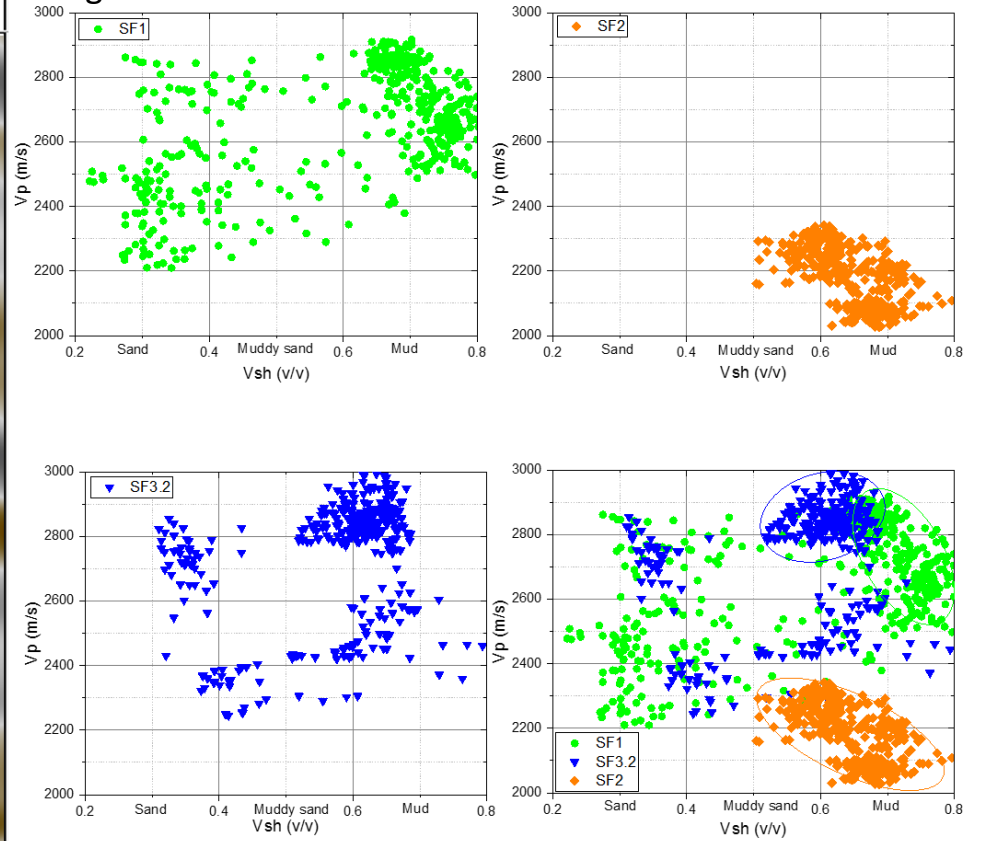
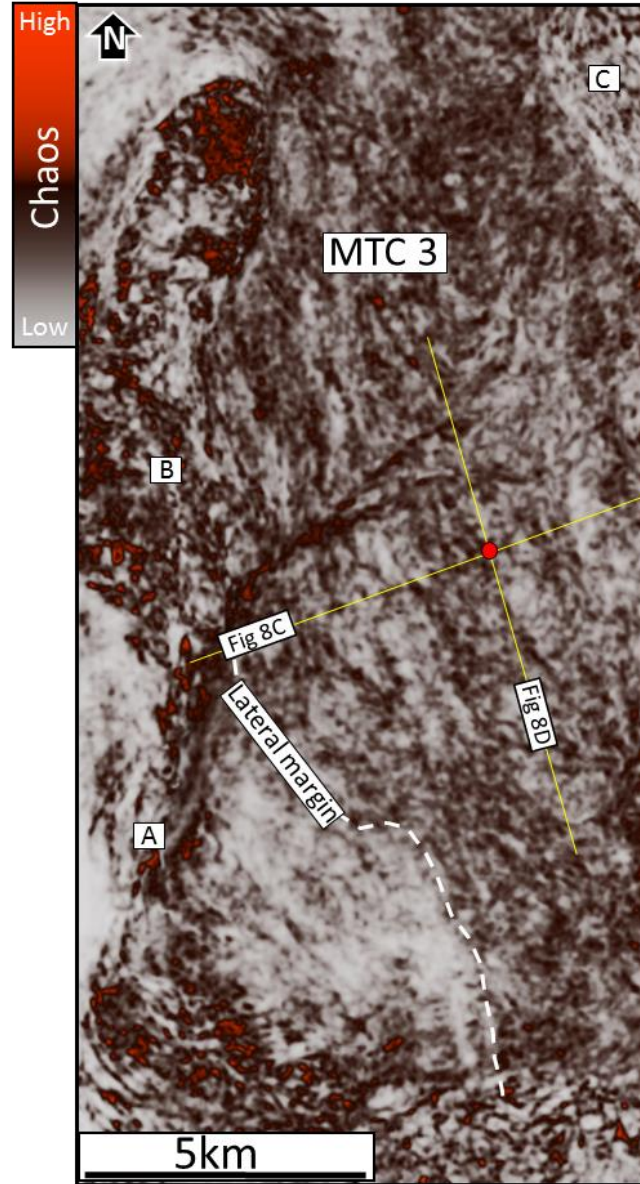


Figure 8A



817

Figure 8B

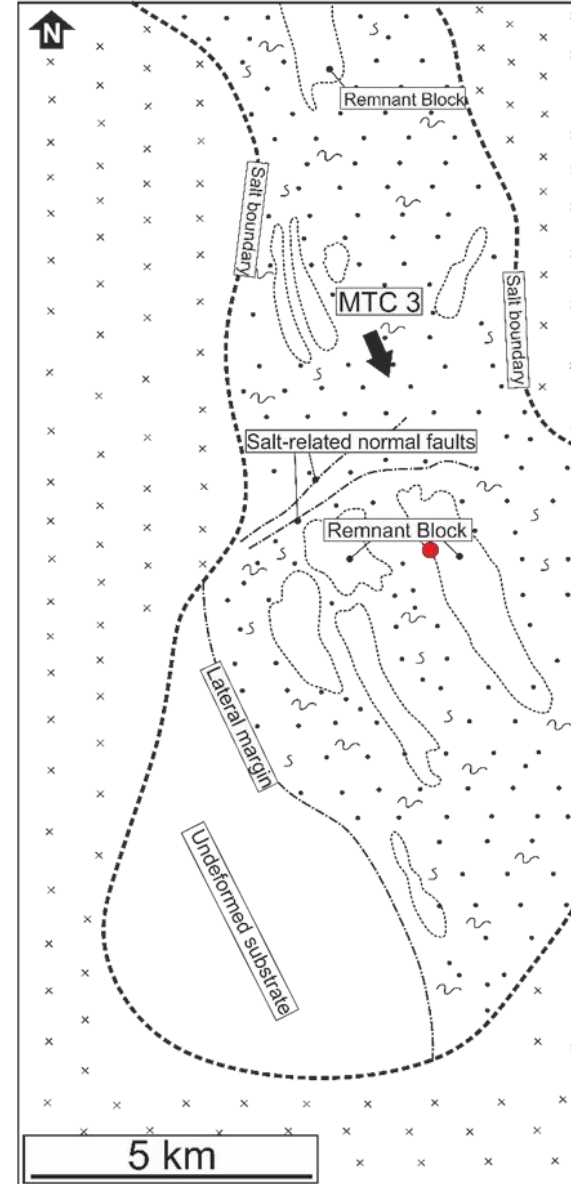


Figure 8C

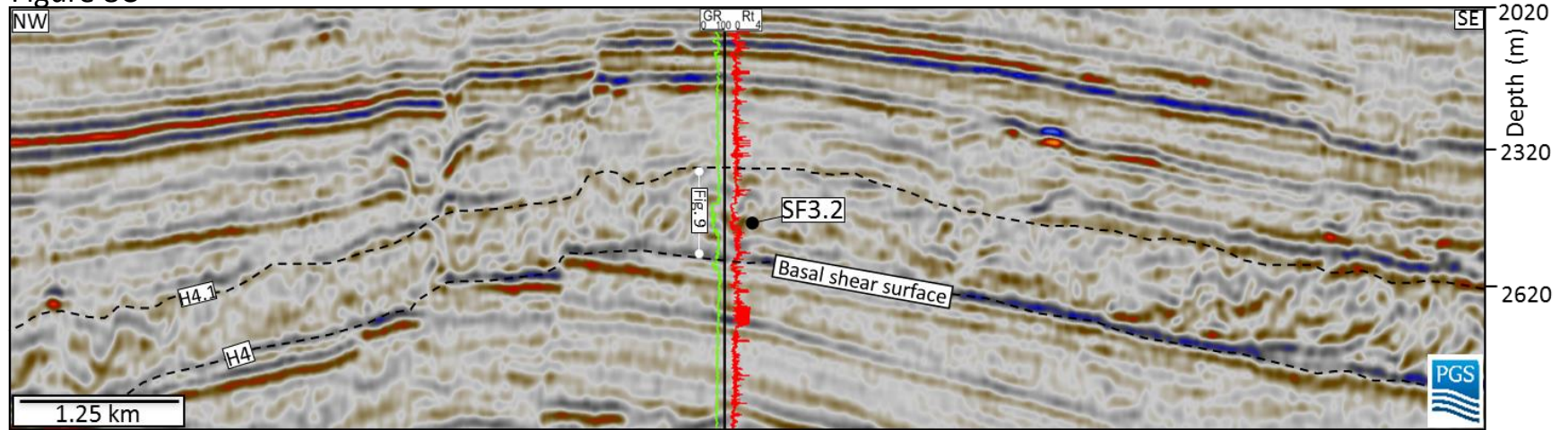
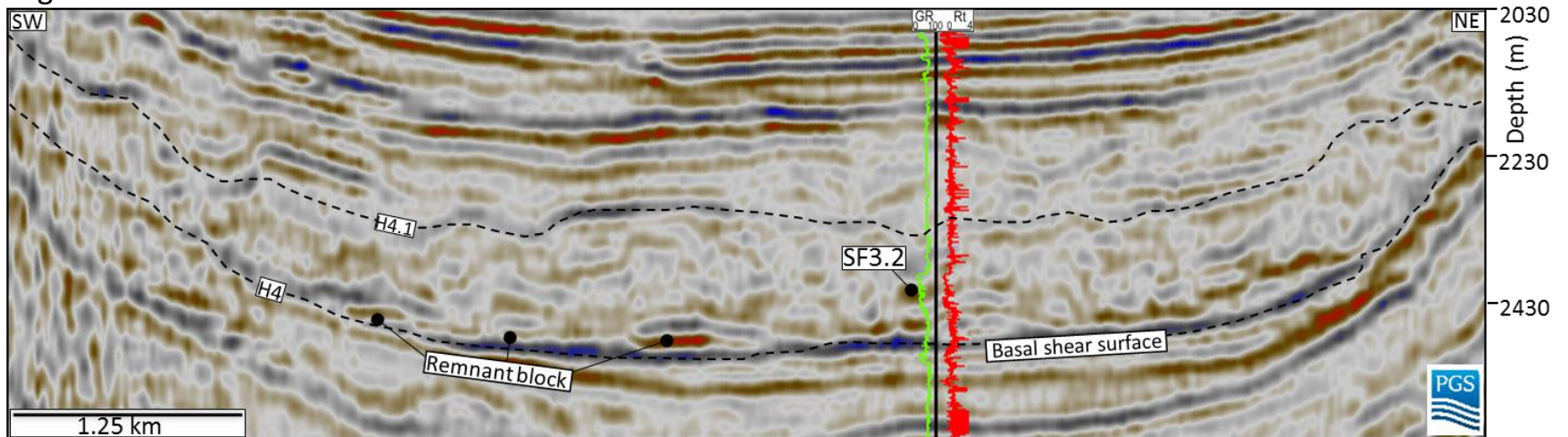


Figure 8D



819

Figure 9A

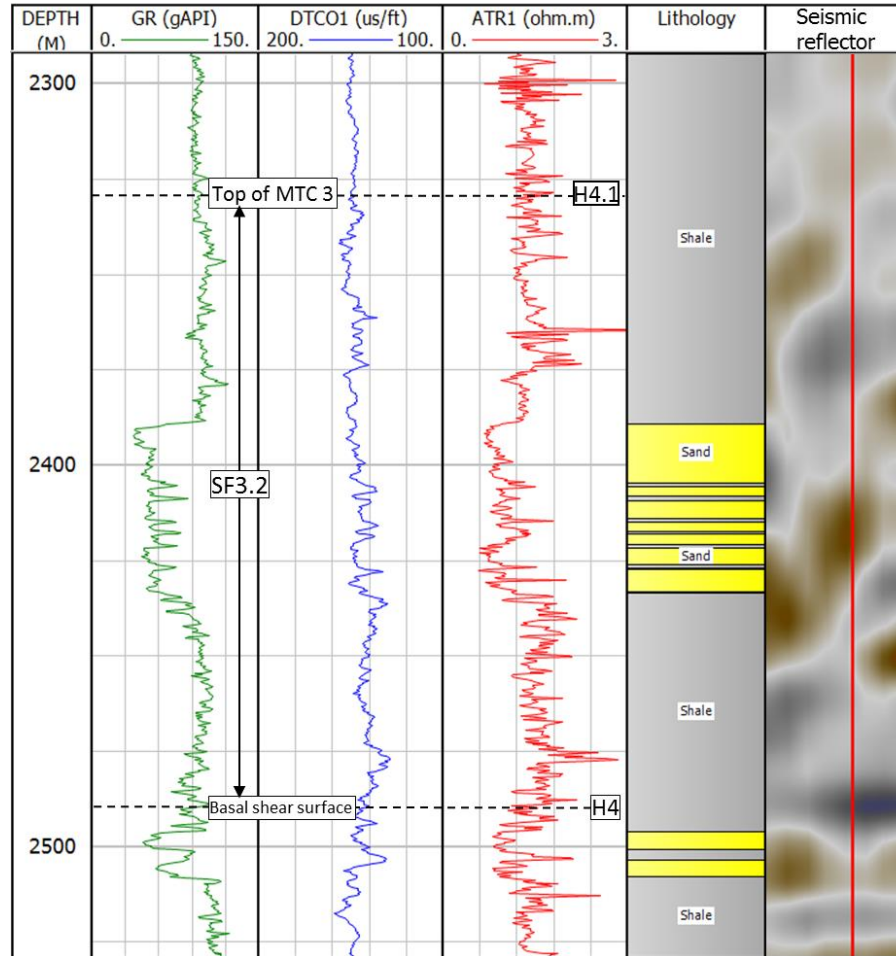
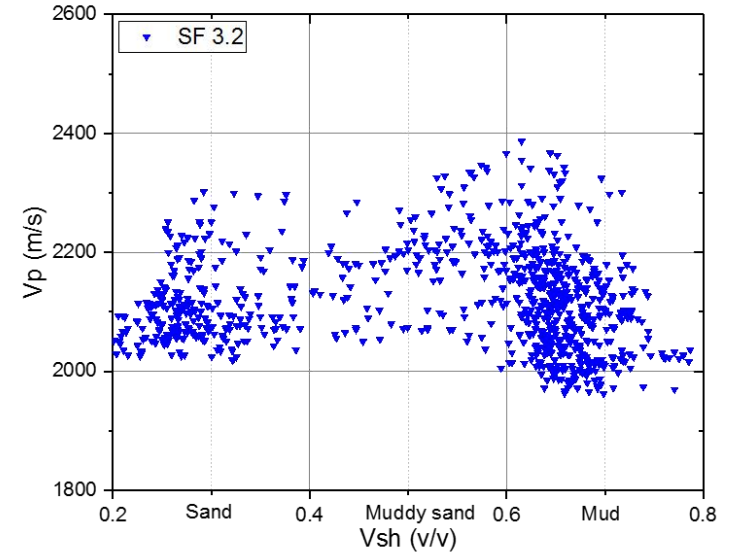


Figure 9B



820

821

Figure 10A

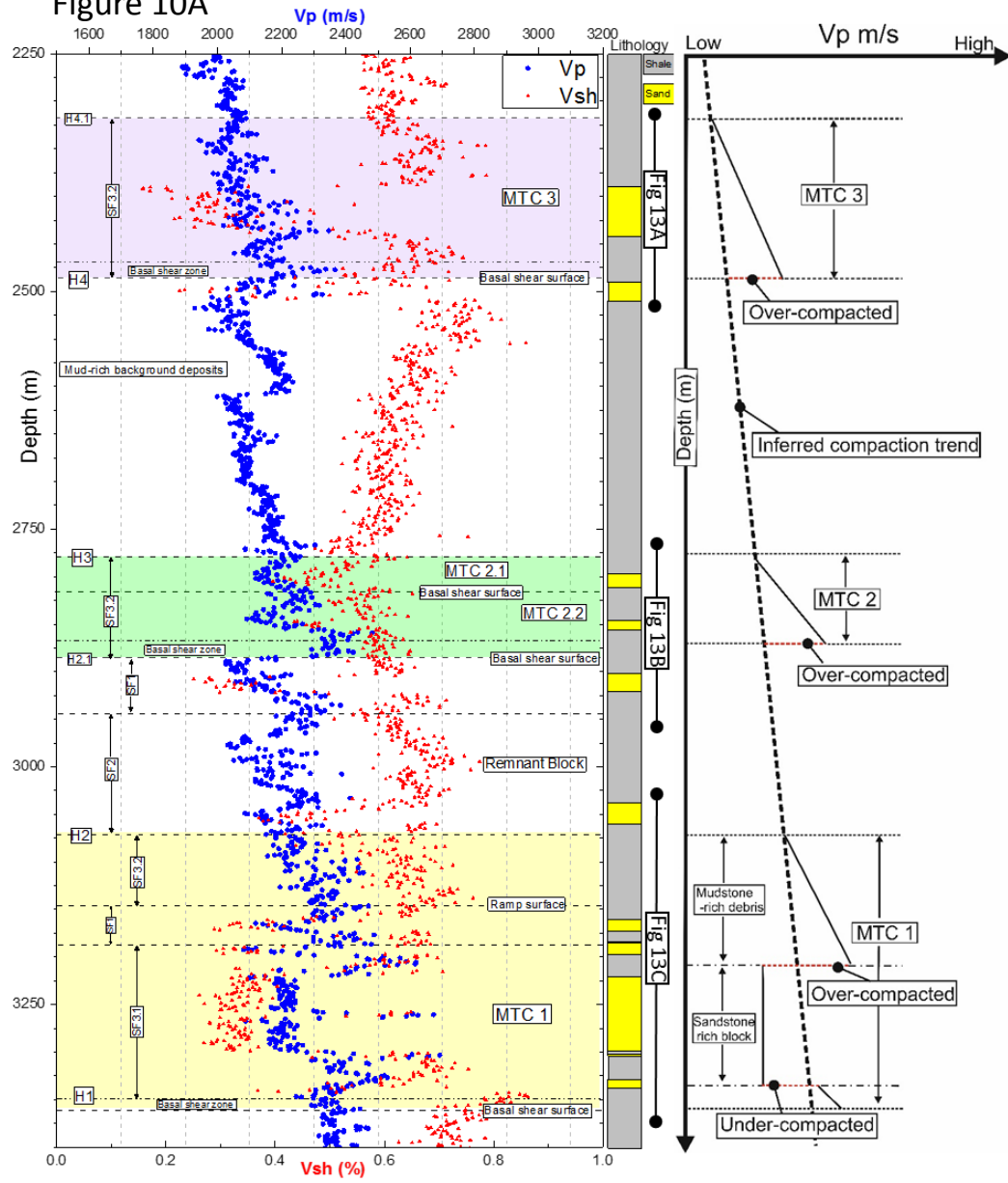
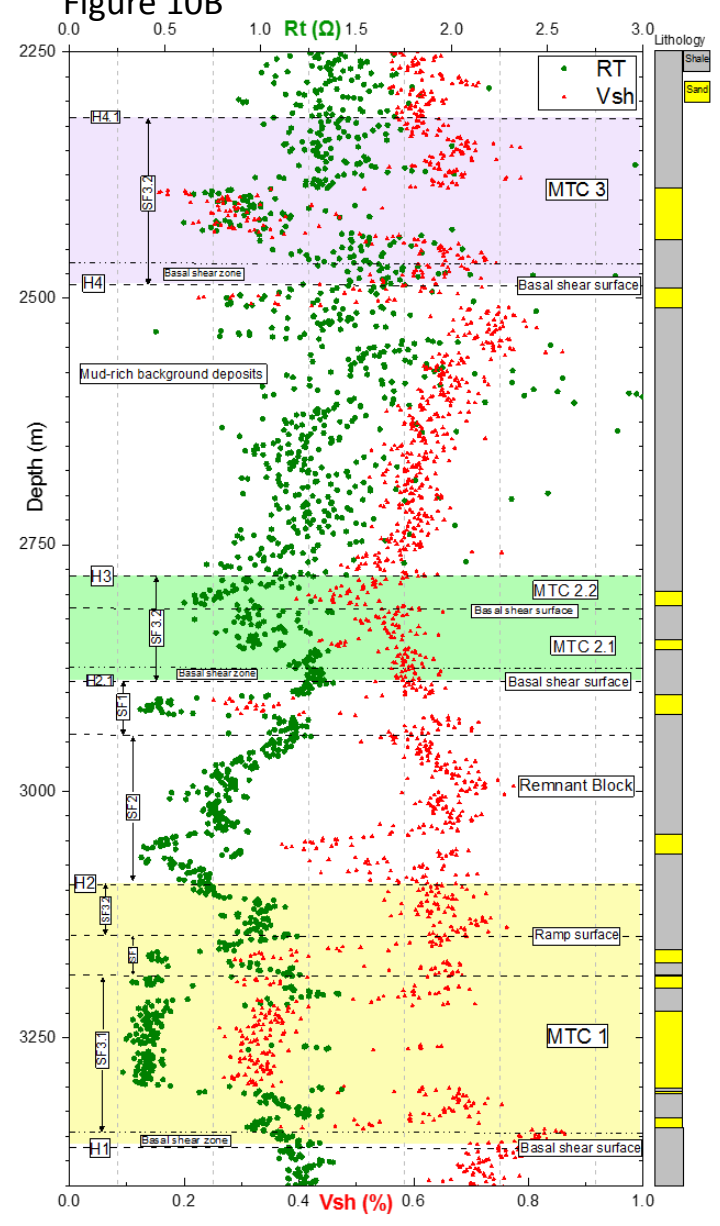
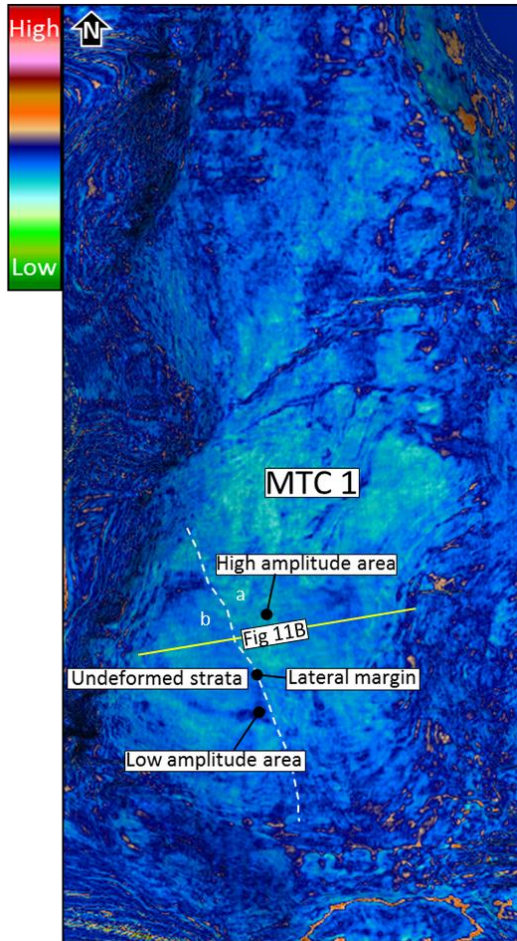


Figure 10B



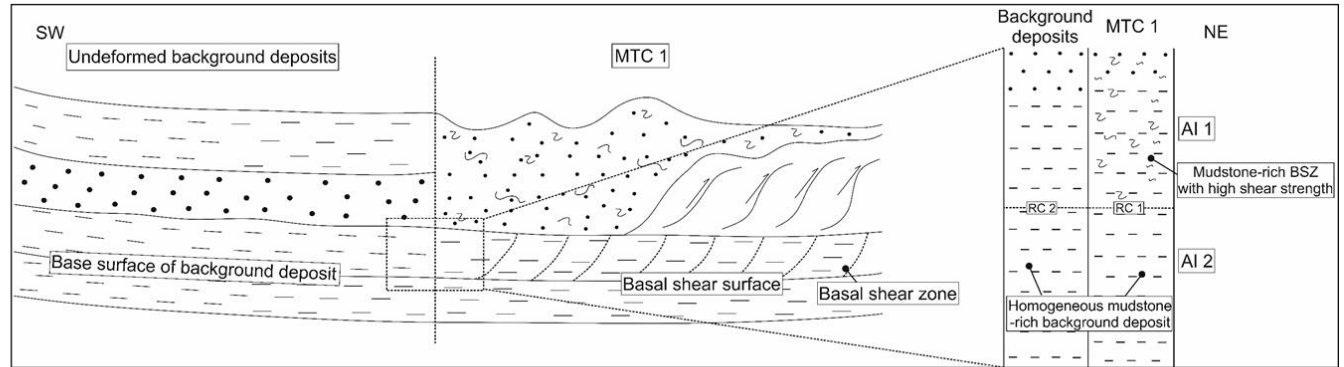
823

Figure 11A



824

Figure 11B



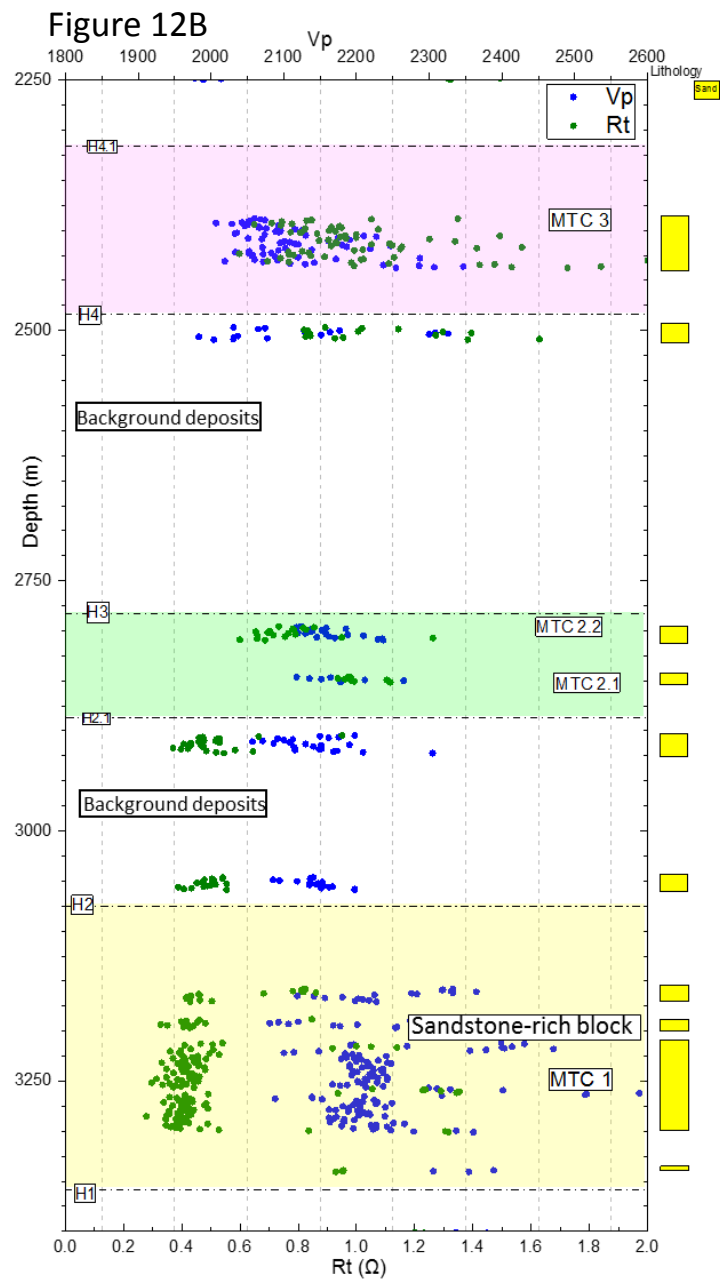
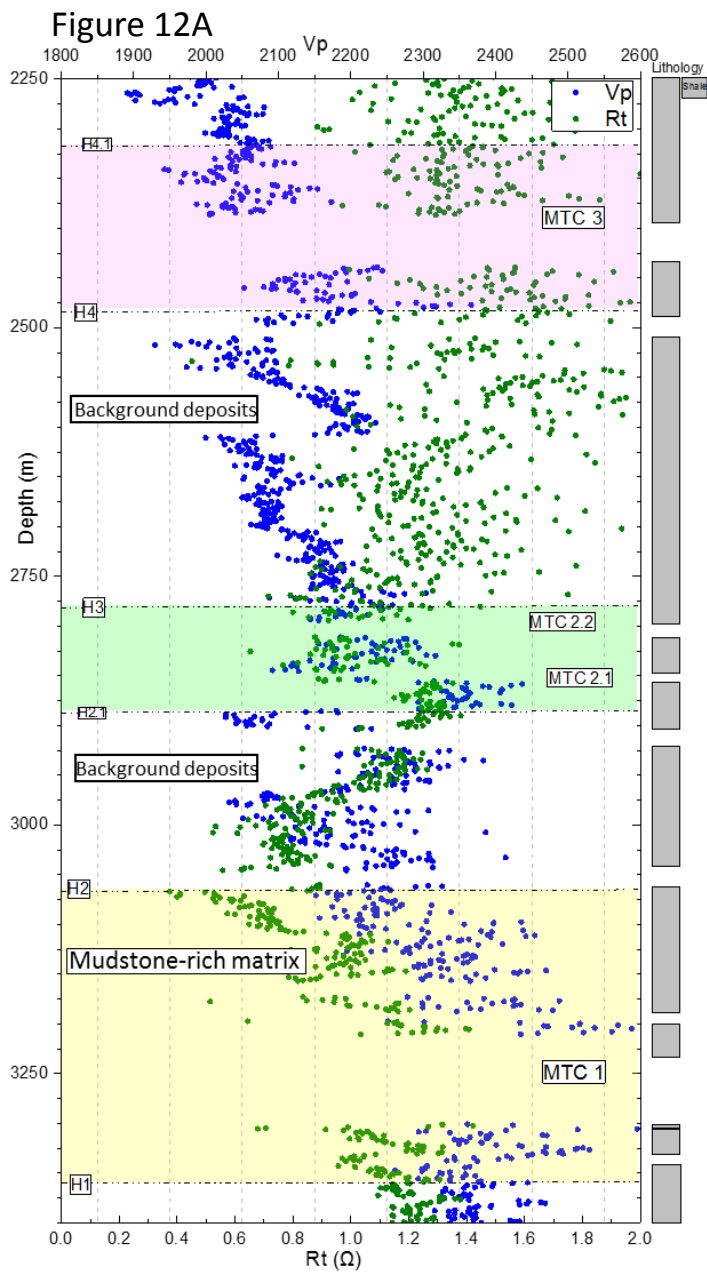


Figure 13A

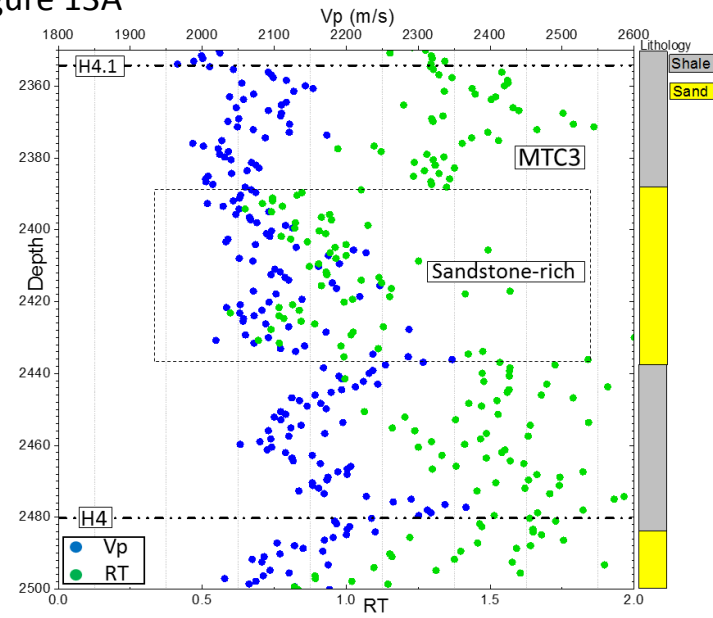


Figure 13B

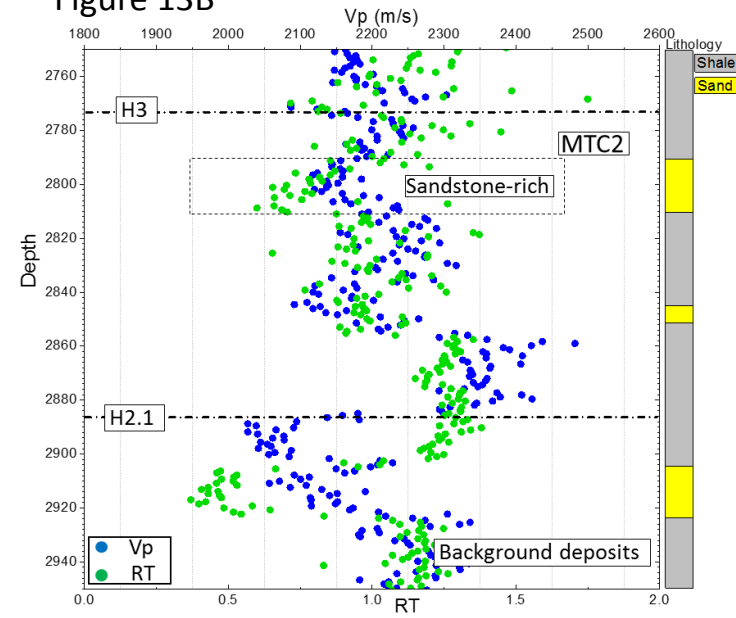
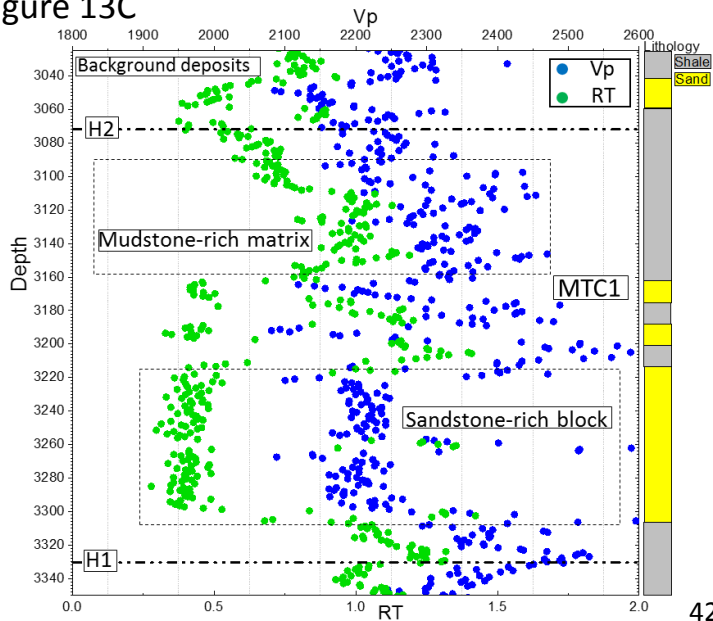
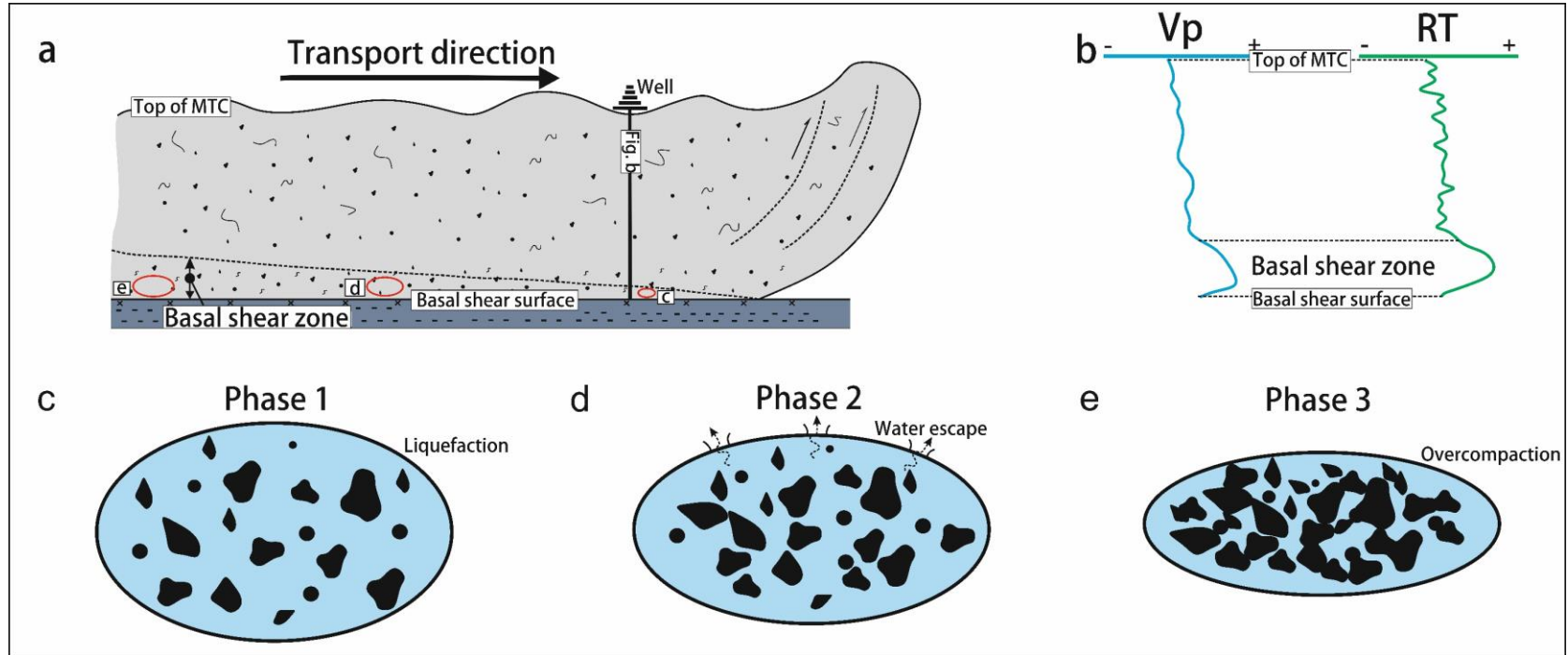


Figure 13C



827

Figure 14



828

829

830

831

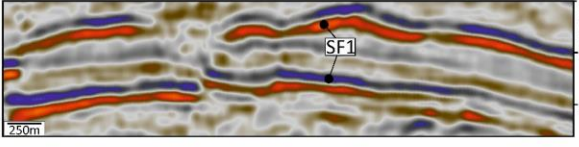

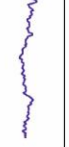
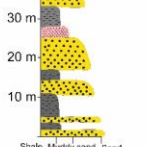
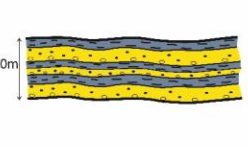
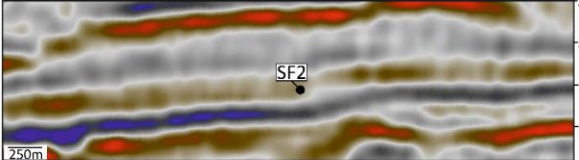

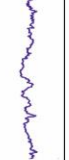
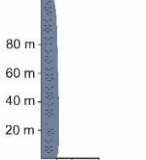
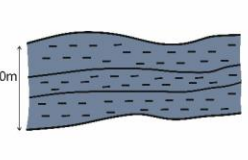
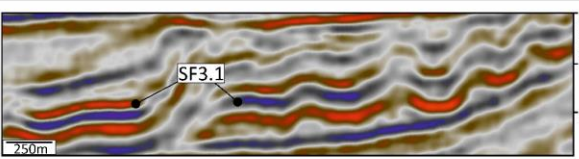

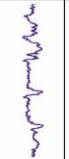
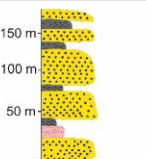
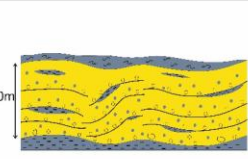
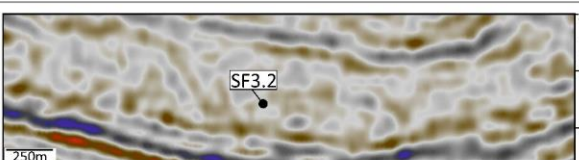

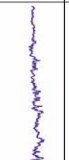
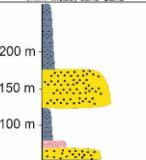
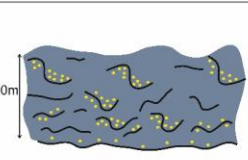
832

833

834

835

Table 1

Seismic facies summary							
Types	Seismic sections	GR	Sonic	Lithology	Schematic facies geometries	Facies characteristics	Depositional Enviroment
SF1						Sub-parallel to parallel, fair continuity, high amplitude reflections; seismic reflectors thinning and pitching out to the end. A fining up-ward trend with block low GR response at base and serrated high GR response at top.	Thinly bedded sandstone-rich and mudstone-rich deposits.
SF2						Sub-parallel to parallel reflections, good continuity, with medium to low amplitude reflections; Constantly serrated high GR response.	Background low energy mudstone-rich deposits.
SF3.1						Less deformed, but more continuous, medium to high amplitude reflections; A fining upward trend GR response at base, a set of blocky low GR response at middle, and a fining upward GR response again at top.	Remobilised and transported sandstone-rich blocks
SF3.2						Chaotic reflections, bad continuity with medium to low amplitude reflections; Constantly serrated high GR response or high GR response interbedded with a set of blocky low GR response.	Mixed highly deformed slump deposits with large sandstone-rich blocks.

836

837

838

839

840 Table 2

MTC	Thickness (m)	Lithology	Thickness of sandstone rich parts (m)
MTC 1	270 m	Large sandstone-rich blocks with mudstone-rich debris	Approx. 180 m
MTC 2.1	77 m	Mudstone-rich debrite with sandstone-rich blocks	Approx. 30 m
MTC 2.2	43 m	Mudstone-rich debrite	Approx. 10 m
MTC 3	182 m	Mudstone-rich debrite with sandstone-rich blocks	Approx. 70 m

841